Estimating radiated noise of cavitating propeller using standard propeller design tools

Auteur : Grimaldos Bautista, Rafael
Promoteur(s) : Rigo, Philippe
Faculté : Faculté des Sciences appliquées
Diplôme : Master : ingénieur civil mécanicien, à finalité spécialisée en "Advanced Ship Design"
Année académique : 2023-2024
URI/URL : http://hdl.handle.net/2268.2/22244

Estimating Radiated Noise of Cavitating Propeller using Standard Propeller Design Tools

submitted on 30 July 2024

by

Rafael GRIMALDOS BAUTISTA | rafael.bautista@uni-rostock.de

Student ID No.: 223202135

First Reviewer:

Prof. Dr. -Ing. Patrick Kaeding

University of Rostock

Chair of Naval Engineering

18059 Rostock, Germany

Second Reviewer:

Dr. -Ing. Dietrich Wittekind

DW-ShipConsult

Lise-Meitner-Str. 9

24223 Schwentinental, Germany

EMship+
Advanced Design

Master Thesis

CONTENT

FIGURES

TABLES

ABSTRACT

The purpose of this work is to investigate the noise radiated by sheet cavitation from marine propellers of different geometric configurations under the same specific operating conditions. The primary objective is to develop a deeper understanding of how variations in propeller design affect the water-borne spectrum, thus providing valuable insights for the acoustic optimization in the design of marine propellers.

The research was conducted in collaboration with DWShipConsult - JASCO Applied Sciences, a company specializing in naval architecture services related to vibrations and noise. Instead of using the traditional Ffowcs-Williams and Hawkings equation, an alternative methodology was introduced based on the manipulation of the sheet cavitation volume. Advanced numerical simulations were performed to measure the quantity of vapour in the propeller blade.

The outcomes of the study demonstrated that the skew angle has a significant impact on the radiated noise due to sheet cavitation. This research is part of the final thesis for the dual master's degree in Mechanical Engineering from the University of Liège and in Naval and Ocean Engineering from the University of Rostock, marking the culmination of a deep and valuable personal and academic learning experience.

1. CONTEXTUALIZATION

1.1. On-board Noise Sources

Noise has been and continues to be a complex issue for engineering companies, particularly in the naval sector. Onboard a ship, there are various sources of vibrations and noise such as machinery (by inducing shell plate vibrations), military and seismic exploration sonars, flow-induced noise from flow over hull and propeller noise. Cavitation noise can occur both in appendages (hydrofoils, bilge keels) and in the propeller.
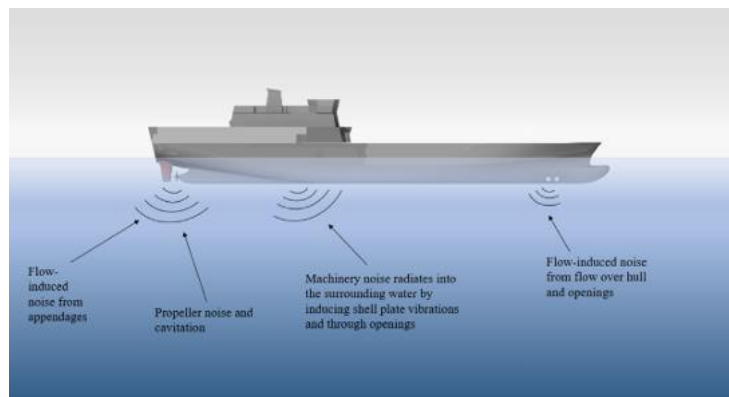
Figure 1. Primary Noise Sources On-Board, furnished by DWShipConsult

This work studies noise produced by cavitating propellers. It has **effects on board**, through structural vibrations (pressure fluctuations, from the water to the structure, and pressure pulses, transferred along the shaft), leading to equipment fatigue and reduced comfort; and **effects under water**, which define the scope of this project and that are of interest both for military vessels, in terms of detection, and for merchant vessels, in relation to the impact on marine life, furnished by DWShipConsult. The project focuses on this last maritime application.

1.2. Why Reduce the Underwater Noise Generated by Shipping Activities?

Many will question the interests in reducing radiated noise generated by shipping activities, beyond the application to the military or even fishing industry, for stealth purposes, however, according to experimental studies in which the noise radiated has been measured, by using hydrophones, it turns out that underwater noise inhibits marine mammals' means of communication and navigation, i.e. shipping noise is masking of biological sound since both frequency signals are within the same range, as shown in Figure 2. The diving problem relates mainly to baked whales, [5].
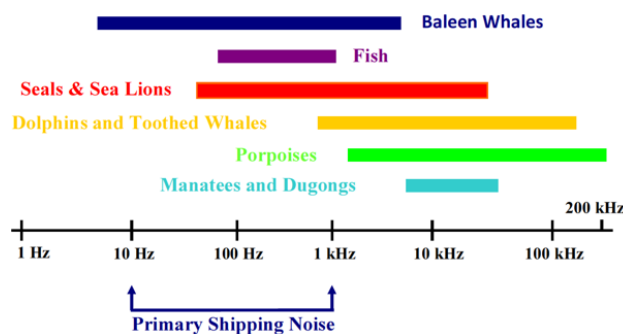
Figure 2. Shipping Noise Frequency Range, furnished by DWShipConsult

Of course, the incessant increase in the number of ships and their growing size exacerbates the problem, which causes baleen whales to lose their sense of direction, panic and ascend rapidly, dying from decompression sickness. Actually, this is a real disaster for the marine ecosystem, as marine mammals are responsible for controlling oxygen (O_2) and carbon dioxide (CO_2) levels and the food pyramid in the environment.

Therefore, the International Maritime Organisation (IMO) treats underwater noise from shipping activities with high priority since 2008 and there is a genuine pressure coming from the United States, seeking to define mitigation measures to be applied on a non-mandatory basis, furnished by DWShipConsult. The sustainable development goals, that 2030 agenda states, provide a blueprint for the transition to a healthier planet and a more just world. In this context, the Sub-Committee on Ship Design and Construction has agreed on an action plan to further prevent and reduce underwater radiated noise from ships, encouraging more research on this issue and its impact on the marine environment, as well as the development of targets and policies for noise reduction, [20].

Figure 3. Sustainable Development Goals, [20]

As shown in Figure 3, IMO aims to conserve life under water, covering all aspects of international shipping to ensure that this vital environment remains safe, and to establish a truly global stakeholder's partnership. Thus, IMO and the United Nations Development Programme (UNDP) plan to launch the GloNoise Partnership, whose aim is to assist developing countries and regions to raise awareness, to build capacity and to collect information to assist the policy dialogue on anthropogenic underwater noise mitigation from shipping. The project is based on IMO's *Guidelines for the reduction of underwater noise from commercial shipping to address adverse impacts on marine life* (*MEPC.1/Circ.833*) published in 7 April 2014.

2. THEORY

2.1. Underwater Radiated Noise

Since the last 70s, the integral formulations solving the Ffowcs Williams-Hawkings (FW-H) equation are the standard approach for the prediction of noise generated by a body moving in a fluid flow and, in particular, propulsion and/or lifting devices based on rotating blades. This methodology represents the base of research and commercial software used by naval industry, in the attempt of providing the shipbuilding sector with effective predictive tools, which to fulfil the stringent regulations of underwater noise emission with, [8].

The FW-H equation represents an extension of the original work of Lighthill and Curle on the aerodynamically generated sound. It may be derived from the fundamental conservation laws of mass and momentum by representing the presence of the body as a discontinuity in the fluid field, as stated in [22],

$$
\begin{aligned}
D^2 p'(x,y) = & +\frac{\partial}{\partial t}[\rho_0 v_n + \rho(u_n - v_n)\delta(f)] \ (\mathbf{1}) \\
& -\frac{\partial}{\partial x_i}[\Delta P_{ij}n_j + \rho u_i(u_n - v_n)\delta(f)] \ (\mathbf{2}) \\
& +\frac{\partial^2}{\partial x_i \partial x_j}[T_{ij}H(f)] \ (\mathbf{3})
\end{aligned}
\tag{1}
$$

where $\mathbf{D}$ is the D'Alembert operator, $\mathbf{T_{ij}}$ is the Lighthill stress tensor, $\mathbf{P_{ij}}$ is the compressible stress tensor, $\mathbf{u_n}$ is the velocity component normal to the surface, $\mathbf{v_n}$ is the surface velocity component normal to the surface, $\mathbf{u_i}$ is the fluid velocity component in x_i direction and $\mathbf{n_j}$ is the unit normal vector pointing toward the exterior region.

$$
D^2 = \frac{1}{c_0^2}\frac{\partial^2}{\partial t^2} - \nabla^2
\tag{2}
$$

$$
P_{ij} = p\delta_{ij} + \mu\left(-\frac{\partial u_i}{\partial x_j} - \frac{\partial u_j}{\partial x_i} + \frac{2}{3}\frac{\partial u_k}{\partial x_k}\right)\delta_{ij} \rightarrow \Delta P_{ij} = P_{ij} - \rho_0\delta_{ij}
\tag{3}
$$

$$
T_{ij} = \rho u_i u_j + P_{ij} - c_0^2(\rho - \rho_0)\delta_{ij}
\tag{4}
$$

Hydro-acoustics is made up of 3 components, collected in Equation (1): **thickness noise (1)**, representing volume displacements effects when surfaces are moving (acting as a **monopole radiator**); **loading noise (2)**, representing load distributions upon the blades (acting as a **dipole radiator**); and **non-linear influences (3)** in the flow field, caused by free turbulence and instantaneous air bubbles which condense from the water in low pressure, as occurs in hydraulic systems (acting as a **quadrupole radiator).**

$$I_m \propto \frac{\rho}{c}\vartheta^4 = \rho\, M_a \vartheta^3 \qquad\qquad I_d \propto \frac{\rho}{c^3}\vartheta^6 = \rho\, M_a^3 \vartheta^3 \qquad\qquad I_q \propto \frac{\rho}{c^5}\vartheta^8 = \rho\, M_a^5 \vartheta^3$$
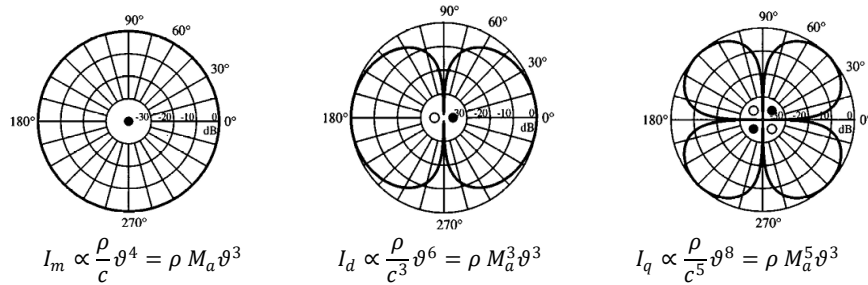
Figure 4. Types of Noise Radiators: monopole (left-hand side), dipole (centre side) and quadrupole (right-hand side), [11]

Generally, the total noise measured experimentally results from the sum of all, but for incompressible cases, monopole and dipole terms are cancelled out, and quadrupole radiator term becomes the attention point, since small cavitation bubbles that quickly implode yield shock waves and deeply modify the baseline acoustic signature of the propeller, even at low revolution rate, [22]. Additionally, the equation reduced to the quadrupole term results in:

$$\frac{1}{c_0^2}\frac{\partial^2 p'}{\partial t} - \nabla^2 p' = \frac{\partial^2}{\partial x_i \partial x_j}(\rho u_i u_j) \qquad (5)$$

Moreover, conventional propellers, commonly installed in merchant ships, present a large cavitation bubble which develops, grows and eventually collapses, moving along the suction side of the propeller according to its motion, increasing and decreasing its volume according to the character of the non-homogeneous wake field, consequence of the hull interaction, that changes the inflow conditions for every propeller blade in the upper region, as shown in Figure 5.
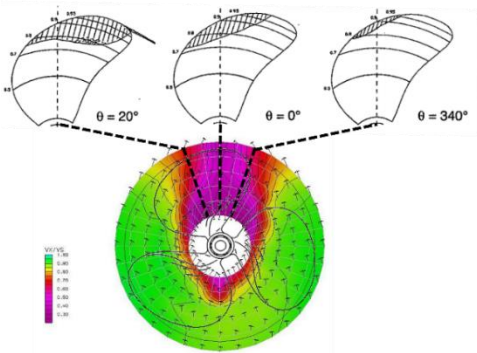
Figure 5. Evolution of Sheet Cavitation under Non-Homogeneous Inlet Flow, furnished by DWShipConsult

This phenomenon is known as **sheet cavitation** and it is considered as they cause the highest dB levels at low frequencies, as shown in Figure 6.
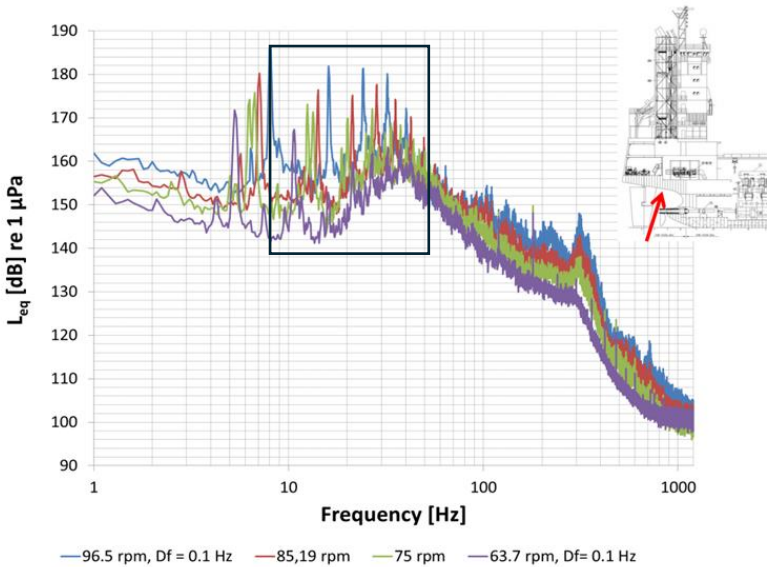
Figure 6. Noise Spectrum of a Container Ship, furnished by DWShipConsult

As a reminder, the creation of bubbles occurs when the pressure drops below vapour pressure at constant temperature, and thus, the parameters involved in the cavitation behaviour are: the <u>behind conditions</u>, which highlights the variation of the pressure field in the propeller blade on its way through the upper part of its circular path, and the <u>revolution rate</u>, through the cavitation number (σ_n) which represents the ratio between the static pressure head and dynamic pressure head, as stated

$$\sigma_n = \frac{p_\infty - p_v}{\frac{1}{2}\,\rho\,n^2\,D^2} \qquad (6)$$

where p_∞ is the pressure in undisturbed fluid and p_v is the vapour pressure in [Pa], n is the revolution rate in [rad/s] and D is the propeller's diameter in [m]. Therefore, lower values imply higher cavitation potential.

All volume fluctuations, described by sheet cavitation, present a very good omnidirectional sound radiation, so that they may act as a **monopole source**, and then all attention will be focused on the cavitation volume curve, in particular to its second derivative, since at low frequencies the volume acceleration is directly related to the pressure signal radiated,

$$p(r,\theta,t) = i\,\frac{Q\,\rho\,c\,k}{4\,\pi\,r}\,e^{i(\omega t - kr)} \qquad (7)$$

where ρ is the fluid density, c is the speed of sound, k is the wave number, r is the distance from source to observation point and Q is the complex source strength, which is related to the second derivative of the cavitation volume, [11].
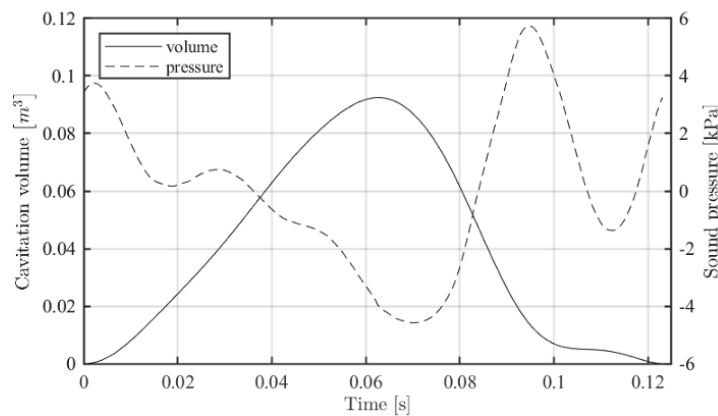
Figure 7. Sheet Cavitation Volume and Pressure Curves, furnished by DWShipConsult

15

The pressure produced by a monopole is the same at all points a distance r from the source, so that the directivity pattern looks like a circle as shown in Figure 4 and the pressure amplitude is no dependent on directivity term, θ. Equation (8) is obtained from [5].

$$|p(r,t)| \sim \frac{\rho \, \ddot{V}(t)}{4 \, \pi \, r} \tag{8}$$

2.1.1. Water-borne Noise Spectrum

In fluids there are only compressional waves (longitudinal), which can be described by **sound pressure** and particle velocity. Inspecting measured data in the frequency domain is the primary part of analysing signals. In noisy environments, Fast Fourier Transform (FFT) analysis can be used to find out which loud tonal are contained in the sound signal. Signal-to-noise ratio (SNR) spectrums are shown in the **logarithmic unit decibels** (dB), so that it is easy to identify wide dynamic ranges,

$$URN[dB] = 10 \log\left(\frac{|p|}{p_{ref}}\right)^2 = 20 \log\frac{|p|}{p_{ref}} \tag{9}$$

where p_{ref} for sound in water is 1μPa, furnished by DWShipConsult.

2.2. Introduction to OpenFOAM

OpenFOAM is an open-source computational fluid dynamics (CFD) software package used for simulating fluid flow, turbulence, heat transfer, and chemical reactions. It provides a robust framework for solving complex fluid dynamics problems through finite volume methods. OpenFOAM's modular structure allows for extensive customization and the development of new solvers and utilities. It supports parallel computing, making it suitable for large-scale simulations, [27].

In the naval industry, OpenFOAM is widely used due to its several applications:

- **Hull Design and Optimization**. Hydrodynamic performance of ship hulls, allowing engineers to optimize designs for reducing drag and improving seakeeping performance.
- **Wave-Structure Interaction**. Simulation of interaction between waves and maritime structures such as offshore platforms and breakwaters, aiding in the design and safety assessment of these structures.
- **Propeller Analysis**. Performance and cavitation characteristics, enabling the design of more efficient propulsion systems, in terms of noise and efficiency.

The methods of approximation (RANS, LES and DNS) are categorized based on the resolution they achieve, ranging from those that estimate turbulent motion to those that achieve precise resolution of each turbulent movement within the fluid, thus escalating computational costs commensurately with the level of detail, [28].

- Reynolds-Averaged Navier Stokes, or **RANS**, methods. They involve averaging the Navier Stokes equations over time to separate the mean flow from the turbulent fluctuations.
- Large Eddy Simulation, or **LES**, methods. They are used to simulate turbulent fluctuations flows by resolving the large-scale turbulent eddies while modelling the effect of smaller scales.
- Direct Numerical Simulation, or **DNS**, methods. A rigorous approach where all turbulent scales in a flow are resolved directly without any turbulence modelling, but it solves the Navier-Stokes equations numerically with very fine spatial and temporal resolutions, capturing even the smallest turbulent eddies down to the Kolmogorov scale.

RANS models are suitable for engineering applications where balance between computational efficiency and accuracy of results is crucial. Thus, they are used here for modelling turbulence.

2.2.1. Cavitation Analysis with Dynamic Meshes

In the cavitating case, the *interPhaseChangeFoam* solver is implemented, supporting the functionality of dynamic mesh motion, designed for incompressible, isothermal immiscible fluids, which are capable of phase change, such as cavitation or surface evaporation/condensation. It handles laminar and turbulent flow and uses the PIMPLE algorithm (merged PISO-SIMPLE) for pressure-momentum coupling, leveraging the strengths of both PISO and SIMPLE methods for pressure-velocity coupling, ensuring robustness in handling transient flows with large time steps, [29]. This approach is supplemented by under-relaxation techniques to secure convergence stability. The flow is governed by the continuity equation

$$\frac{\partial u_i}{\partial x_i} = 0 \tag{10}$$

coupled with the Navier-Stokes equation, also known as momentum equation,

$$\frac{\partial u_i}{\partial t} + \frac{\partial u_i u_j}{\partial x_j} = -\frac{1}{\rho}\frac{\partial p}{\partial x_i} + \frac{\partial}{\partial x_j} \nu \left(\frac{\partial u_i}{\partial x_j} + \frac{\partial u_j}{\partial x_i} \right) + S_i \tag{11}$$

where $x_i = (x,y,z)$ are the Cartesian coordinates and $u_i = (u,v,w)$ are the components of the velocity. The left-hand side of the momentum equation represents the inertial of the flow (composed of unsteady acceleration and non-linear convection of momentum) driven by external forces, that can be in the form of pressure gradients, viscous forces and body forces, (which constitute the right-hand side of the momentum equation). The source term S_i include the gravitational force and an oscillating source of momentum in order to drive an oscillatory flow. Up to this point, the solver *pimpleFoam*, which is designed for single-phase flows, encompasses the aforementioned equations.

The cavitating flow is a mixture of two species, vapour and liquid, behaving as one (homogeneous mixture: idealization of a multiphase flow), so that they share the same instantaneous velocity and pressure fields. The phase interface is taken care of using a Volume of Fluid (VoF) approach, a numerical technique that can model two or more immiscible fluids by tracking the interface in each cell throughout the computational domain, [23].

Cavitation is modelled by certain **mass transfer models**: Merkle, Kunz or Schnerr-Sauer. Merkle and Kunz models are very similar and they consider the vaporization is proportional to the amount by which the pressure is below the vapour pressure. However, in contrast to Schneer-Sauer model, condensation and vaporization are not symmetrical, [19].

The modelling of the interphase mass transfer rate ($\dot{m}$) is the core of any cavitation model, so that an appropriate source term is needed to account for the phase passage. **Schnerr-Sauer** cavitation model is based on transport equation, which uses different source terms to represent condensation and vaporization process to simulate mass transfer between gas and liquid.

$$\dot{m} = \dot{m}_c + \dot{m}_v \tag{12}$$

The expression of **mass source term** for condensation rate and vaporization rate are as follows

$$\dot{m}_c = C_c 3 \frac{\rho_v \rho_l}{\rho_m} \frac{\alpha(1-\alpha)}{R} \sqrt{\frac{2}{3} \frac{|p - p_v|}{\rho_l}} \, sgn(p_v - p) \tag{13}$$

$$\dot{m}_v = C_v 3 \frac{\rho_v \rho_l}{\rho_m} \frac{\alpha(1-\alpha)}{R} \sqrt{\frac{2}{3} \frac{|p - p_v|}{\rho_l}} sgn(p_v - p) \tag{14}$$

where vaporization can be unbalanced with respect to condensation by modifying C_c and C_v parameters. The model is based on bubble dynamics and the amount of vapour in a control volume is calculated from the number of nesting bubbles and average radius of the bubbles.

The vapour fraction is expressed as follows

$$\alpha = \frac{n_0 \frac{4}{3}\pi R^3}{1 + n_0 \frac{4}{3}\pi R^3} = \frac{volume\ vapour}{total\ volume} \tag{15}$$

where n_0 is the vapour nuclei concentration per unit and R is the initial radius of the nuclei. Suggested values are $n_0 = 10^9$ - 10^{13} N/m^3 and $R = 10^{-4} - 10^{-8}$ m, as stated in [19].

In the VoF approach, the physical properties of the fluid are scaled by a volume fraction (γ), with $\gamma=1$ corresponding to water

$$\rho = \gamma\rho_l + (1-\gamma)\rho_v \tag{16}$$

$$\mu = \gamma\mu_l + (1-\gamma)\mu_v \tag{17}$$

where

$$\gamma = \frac{volume\ liquid}{total\ volume} \tag{18}$$

Therefore, an additional transport equation for the volume fraction needs to be incorporated,

$$\frac{\partial \gamma}{\partial t} + \frac{\partial(\gamma\ u_i)}{\partial x_i} = \frac{\dot{m}}{\rho_l} \tag{19}$$

into the filtered equations of continuity and momentum, shown below.

$$\frac{\partial \rho}{\partial t} + \frac{\partial(\rho\ u_i)}{\partial x_i} = 0 \tag{20}$$

$$\frac{\partial(\rho\ u_i)}{\partial t} + \frac{\partial(\rho\ u_i u_j)}{\partial x_j} = -\frac{\partial p}{\partial x_i} + \frac{\partial}{\partial x_j}\mu\left(\frac{\partial u_i}{\partial x_j} + \frac{\partial u_j}{\partial x_i}\right) + S_i \tag{21}$$

InterPhaseChangeFoam solver provides as primary results fields velocity in [m/s], phase volume fraction and kinematic pressure in [m^2/s^2], as OpenFOAM defines the momentum equation such that the modelled pressure is p/ρ. As derivative results i.e. can be computed based on primary results and supplementary models, for instance, it provides forces on the propeller, [29].

2.2.2. Turbulence Model

The Reynolds stresses, which define viscous forces in the momentum equation, are expressed in terms of the turbulent viscosity (μ_T). Depending on how it is predicted, different models will be used, each adding more or fewer equations. Among the most popular are the 2 equation models, which account for both convective and diffusive effects of turbulent energy. Since we are interested in effects near the propeller surface, k-ε model will be used, whose transport equations are expression (22) and expression (23). For turbulent kinetic energy (k),

$$\frac{\partial(\rho\,k)}{\partial t} + \frac{\partial(\rho\,k\,u_i)}{\partial x_i} = \frac{\partial}{\partial x_j}\left[\left(\mu + \frac{\mu_T}{\sigma_k}\right)\frac{\partial k}{\partial x_j}\right] + P_k + P_b - \rho\varepsilon - Y_M + S_k \tag{22}$$

where $\mathbf{P_K}$ is the production of turbulent kinetic energy due to mean velocity shear, $\mathbf{P_b}$ is the production of turbulent kinetic energy due to buoyancy, $\mathbf{S_k}$ is the user-defined source and $\boldsymbol{\sigma_k}$ is the turbulent Prandtl number for k. And, for turbulent dissipation rate (ε),

$$\frac{\partial(\rho\,\varepsilon)}{\partial t} + \frac{\partial(\rho\,\varepsilon\,u_i)}{\partial x_i} = \frac{\partial}{\partial x_j}\left[\left(\mu + \frac{\mu_T}{\sigma_k}\right)\frac{\partial \varepsilon}{\partial x_j}\right] + C_{1\varepsilon}\frac{\varepsilon}{k}(P_k + C_{3\varepsilon}P_b) - C_{2\varepsilon}\rho\frac{\varepsilon^2}{k} + S_\varepsilon \tag{23}$$

where $\mathbf{C_1}$, $\mathbf{C_2}$ and $\mathbf{C_3}$ are model coefficients that vary within k-ε turbulence models, $\mathbf{S_\varepsilon}$ is the user-defined source and $\boldsymbol{\sigma_\varepsilon}$ is the turbulent Prandtl number for ε, [30].

2.3. Signal Processing

The size of the FFT, along with the sampling frequency used, will provide with two fundamental pieces of data to understand the information that the measurement will show: the **time constant** and the **frequency resolution**. The time constant (Δt) is simply the time it takes to record enough samples for an FFT of a specific size at a specific sampling rate (f_s). Larger time constant provides more detailed frequency resolution, often excessively detailed at high frequencies, but at the cost of less detailed temporal resolution. The frequency resolution (Δf) indicates from which frequency the data will be shown, and how often it will take samples.

$$\Delta t = \frac{N}{f_s} \tag{24}$$

The **frequency resolution** is the inverse of the time constant, in such a way that the better one of the two variables is, the worse the other one becomes. **To capture low frequencies of a signal where higher tonal components are not of interest**, a lower frequency resolution is more interesting. This means using a larger FFT size and a lower sampling frequency, which allows reducing high-frequency noise that could interfere.

$$\Delta f = \frac{f_s}{N} = \frac{1}{\Delta t} \tag{25}$$

By filtering the pressure signal with a **Gaussian filter**, which defines a probability distribution for noise, has the advantage that the attenuation of higher frequency components is more effective than with moving-average filters. One can control the effectiveness of the low-pass nature of the filter by adjusting its width, also known as **filter size** (σ). During lowpass filtering, greater weight values increase the filter's effects, [26].

3. OBJECTIVES

The objective of this thesis focuses on the study of noise radiated by cavitating marine propellers, behind a non-uniform wake field, in particular that produced by sheet cavitation which it has become clear that is the main propeller noise source at low frequencies. A study methodology is proposed in a low-frequency broad band particularly characterized by cavitation phenomena to reduce noise levels by between 10 to 15 dB, by focusing on the cavitation volume curve, in particular the collapse stretch which is supposedly the most critical in terms of pressure variation and hence noise generation [5].

Previous studies [21] point to the skew angle (θ_s^{tip}) as a key geometric parameter in controlling cavitation volume evolution. Therefore, two propellers' configurations, which differ just in this parameter, have been modelled using a computer-aided design (CAD) tool and simulated in OpenFOAM, as computational fluid dynamics (CFD) software, in order to compare the evolution of the cavitation bubble and their corresponding water-borne noise spectrum.

Finally, the pressure field profile in the blade has also been compared in order to check that this problem can also be covered by a single-phase RANS model or potential flow solvers.

4. PRE-PROCESSING

This section describes the pre-processing procedure, covering the design and characteristics of the propellers, description of the simulation domain, definition of the inflow wake field and boundary conditions.

4.1. Modelling of Propeller Geometries

The E779A propeller is analysed subjected to a non-homogeneous wake inflow resulting from a single-screw container ship. It is a four-bladed, fixed-pitch, right-handed propeller characterized by a very low skew, originally designed in 1959 for a ferry, but never built in full-scale. It was chosen as reference model for the Italian Navy Cavitation Tunnel and a comprehensive series of data is available from an experimental programme performed at INSEAN, [16]. The propeller rake is positive if backward, i.e. blade tip away from ship hull. In Table 1 are presented the main geometrical parameters of the E779A model.

Table 1. Characteristics of E779A Propeller, [16]

Parameter	Value
Diameter	$D_p = 22.73$ [cm]
Number of Blades	$Z = 4$
Pitch Ratio (nominal)	$P/D = 1.1$
Expanded Area Ratio	$EAR = 0.689$
Rake (nominal)	$i = 4°35\,'$ (forward)
Skew angle at blade tip	$\theta_s^{tip} = 4°48\,'$ (positive)
Hub diameter (at prop. ref. line)	$D_h = 45.53$ [mm]
Hub length	$L_h = 68.30$ [mm]
N [rpm]	1830
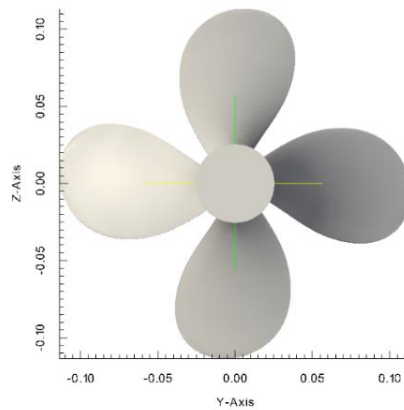
Figure 8. Geometry with Conventional Blade Profile (plane YZ)

The development of advanced computational tools is required especially in modern propeller design, where for reducing noise generation there is a continuous trend towards an increased complexity of the blade geometry, primarily due to the low skew of marine propellers. Highly skewed propellers lengthen the duration of suction-side sheet cavitation and then reduce the volume acceleration, while maintaining propeller efficiency.

As shown in Figure 9, the skew angle of a particular section is the tangential component of the angle formed on the propeller blade between the propeller reference line and a radial line from the propeller origin, passing through the mid-chord of the considered section at radius r. The propeller skew angle is the largest spanning angle between two lines from the propeller origin running through the various mid-chords of the radial blade sections, [9].
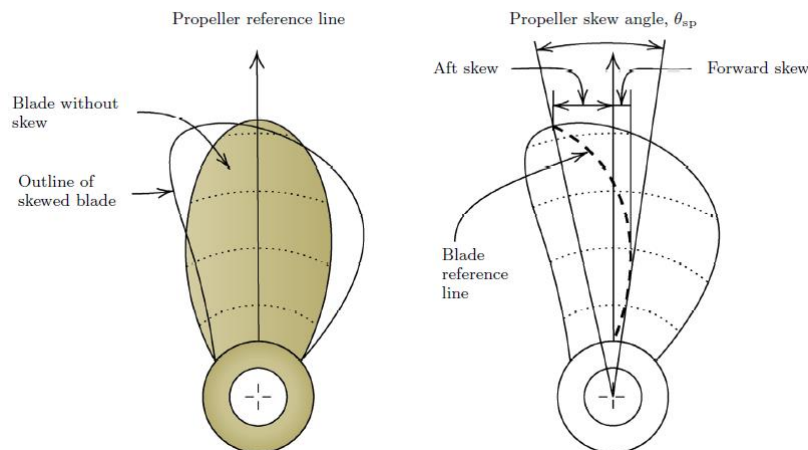
Figure 9. Skewed Propeller Blade Definition, [9]

The centreline of each blade is then swept curvilinearly backward of the direction of rotation, and as a result, the contour of the blade is not radially symmetric around its centreline. The geometry was modelled by shifting each blade section in circumferential direction, as shown in Figure 10, according to the skew angle, which is increased up to $\theta_s^{tip} = 35°$ to have a realistic skew propeller, but higher skews are feasible.
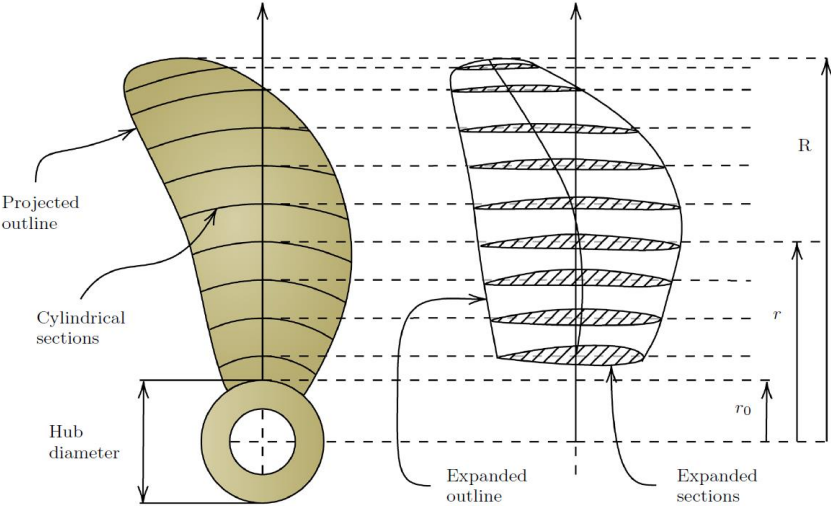
Figure 10. Unwrapping the Radial Sections, [9]
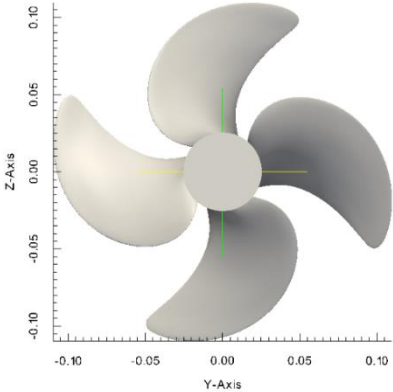
Figure 11. Geometry with High-Skew Angle Blade Profile (plane YZ)

The geometry of the propellers from a side view details other parameters such as the shaft length, rake and pitch, the latter is especially important regardless of the pressure field generated on the blade. Reducing the pitch under the same operating conditions modifies the cavitation behaviour, potentially even causing cavitation on the pressure side. Therefore, it is necessary to clarify that the only geometric parameter that has been modified is the skew, so that both propellers are simulated under the same propulsive properties.
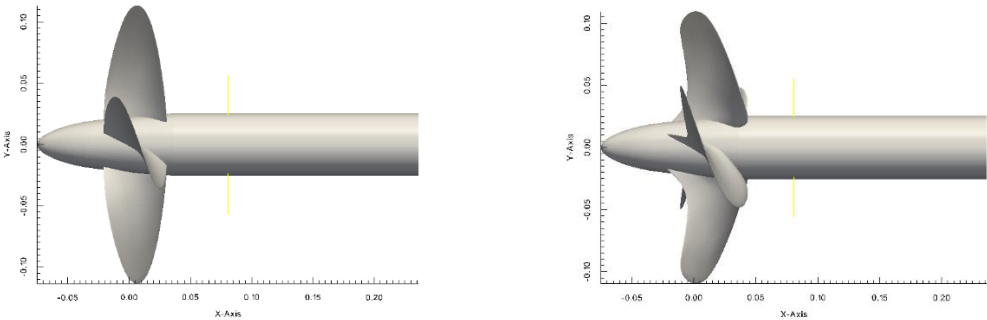
Figure 12. Geometry Configurations (plane XZ)

4.2. Definition of the Simulation Domain

Meshing is of paramount importance in computational fluid dynamics, and a balance is sought between accuracy, to achieve acceptable results, and computational cost. When you need to mesh a cylindrical object, such as propellers, one of the tricks to get a good mesh is to use cylindrical background mesh. The domain is then defined by a cylinder (*outerCylinder*), whose inlet is located at a distance that avoids uncertainties in the calculations that may modify the wake field and the outlet at a distance that allows the full development of the resulting flow. The simulation domain should not influence the results, so a common practice when simulating propellers is to use a sufficiently large diameter of the cylinder.

Table 2. Dimensions of Simulation Domain

Geometry	Value	Length
outerCylinder	4 D_p	7 D_p
middleCylinder	2.5 D_p	4.5 D_p
innerCylinder	1.5 D_p	0.5 D_p

One of the most common strategies in CFD is to refine the mesh where it is believed that the solution may be more complex. In this particular case, the mesh will be refined around the propeller to capture the cavitation volume. Moreover, mesh transitions must be gradual and therefore different refinement zones are used (*middleCylinder* and *innerCylinder*), which are given a higher density of cells as they approach the area of interest.
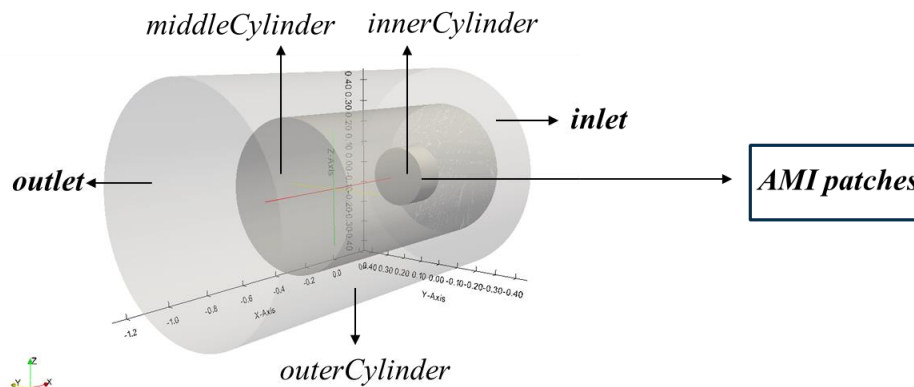
Figure 13. Domain of Simulation

The rotational motion of the propeller is represented by a **dynamic sliding mesh**, whose solution is interpolated back-and-forth between topologically separated regions, [31]. The mesh interface is a patch type called *Arbitrary Mesh Interface*, or AMI, and in order to reduce interpolation errors, the meshes should be similar in the master (AMI 1: rotating patch) and slave (AMI 2: fix patch) patches. Prior to the mesh interface definition, the *innerCylinder* must be defined as a *cellZone* and *faceZone*, so that *createBaffles* tool identifies such zone. The revolution rate of the rotating patch is set to the propeller operating point, i.e. 30.5 rev/s which is equivalent to 192 rad/s.
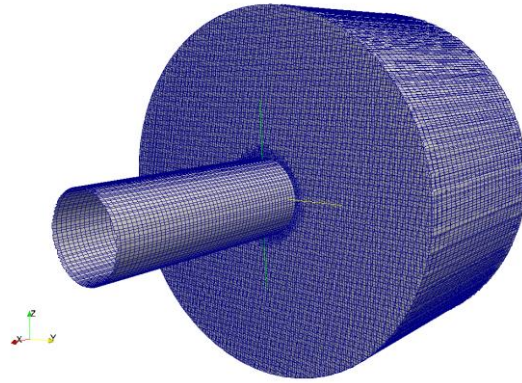
Figure 14. Dynamic Sliding Mesh: Arbitrary Mesh Interface (AMI1 and AMI2)

By using cylindrical mesh, cell count is usually significantly lower and the quality mesh is higher, compared to a block mesh, obtaining a skewness below 5, which is quite admissible.

The skewness is defined as the difference between the shape of the cell and the shape of a quadrilateral cell of equivalent volume [24]. Highly skewed cells can decrease the accuracy and destabilize the solution, so that solver controls should be adjusted such as reducing under-relaxation factors. Geometrically, it is the deviation of the vector **d** that connects the two cells **P** and **N**, from the face centre **f**. The deviation is represented with **Δ** and **f$_i$** is the point where the vector **d** intersects the face **f**, [25]. Basically, it affects the interpolation of the cell centered quantities to the face centre **f**.
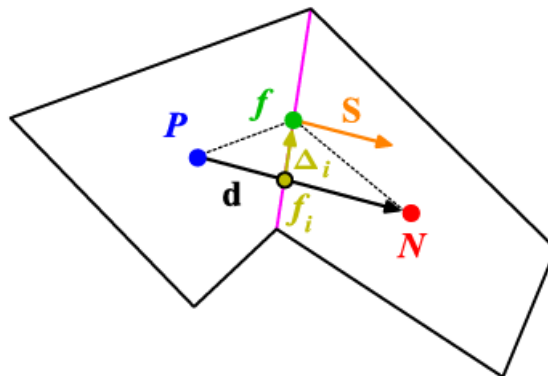
Figure 15. Mesh Skewness, [25]

A typical error that must be reviewed is 0 as minimum weight on AMI interfaces, since in case of sliding meshes, it should be higher than 0 for any relative position of the source/target patches. A mitigation of the problem can be achieved with a coarse mesh or by specifying *lowWeightCorrection* equals to 0.3, when a higher cell density is required, so that when a weight falls below 0.3 a *zeroGradient* boundary condition is applied to those faces, [19]. Figure 16 clearly explain the definition of that weight being discussed.
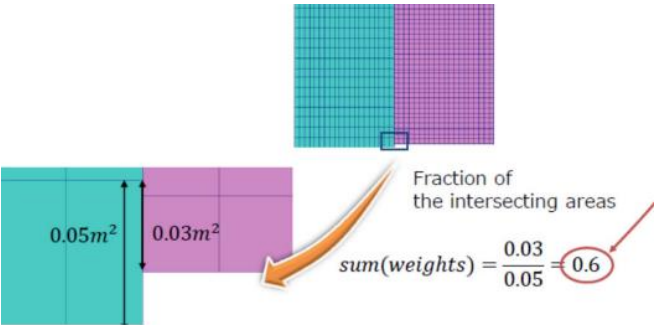
Figure 16. Definition of AMI Interface Weight, [19]

4.3. Setting the Wake-field Inflow

As for the wake field shown in Figure 17, it represents the resulting flow around a single-screw ship moving at 6.22 m/s (12 knots), although the velocity that reaches the propeller is reduced due to the hull interaction. The non-uniform inflow is defined by a tabular format with radial, axial and tangential velocity components, as shown in Appendix 2. **Velocity Components File**, and it is stored in a folder named *boundaryData* in cartesian coordinates (located in file *points*) and velocity components (located in file *U*). The mapping onto the actual mesh is done by the *timeVaryingMappedFixedValue* velocity field condition set up at the inlet.
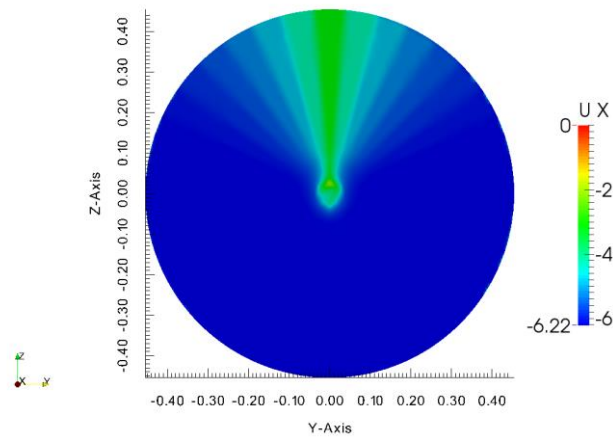
Figure 17. Inflow: Wake-Field from a Single Screw Ship

Narrower wakes further reduce the area in which sheet cavitation occurs, so that pressure changes are more abrupt. Another path that research could take is to study the impact of the wake on the cavitation bubble. The number of harmonics is strongly related to the shape of the pulses and, for sheet cavitation on the blade, the pulse shape is related to the gradient of the wake. Then, the higher the gradient of the wake the more harmonics. The limit of harmonics is set by the number of harmonics that can be clearly distinguished above the continuous spectrum.

In order for the information to be read and transferred through the domain, so that it reaches the propeller properly, the domain is refined mainly in the inlet region to prevent velocity gradients from shooting up.
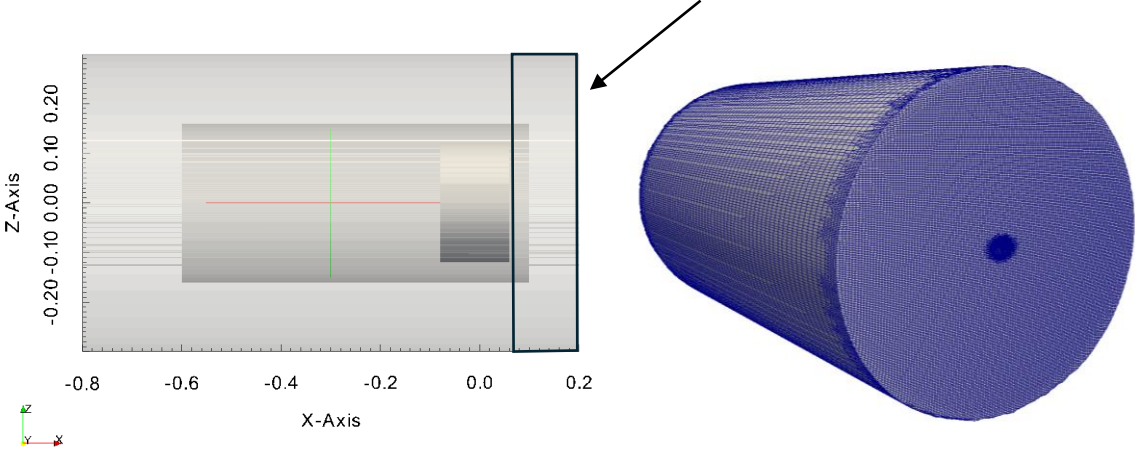
Figure 18. Refinement Region: Inlet Boundary

Therefore, the mesh of the simulation domain at the inlet is refined and the non-uniform wake field is implemented with the propeller, as shown in Figure 19.
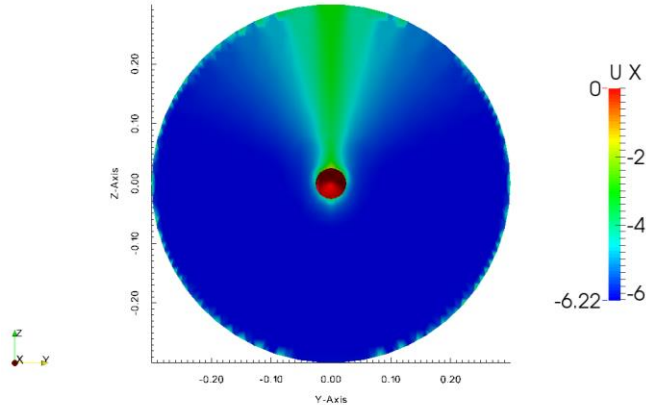
Figure 19. Inflow: Wake-Field from a Single Screw Ship with Propeller Geometry

4.4. Definitive Mesh.

4.4.1. Internal Mesh

By performing cuts according to the XY and YZ planes, it is observed that cell volume is smaller in areas closer to the propeller. The edge size is specified in terms of percentage of the propeller diameter (D_p): in the *outerCylinder* region is 24%D_p, in the *middleCylinder* region is 12 %D_p and in the *innerCylinder* region is 6%D_p.
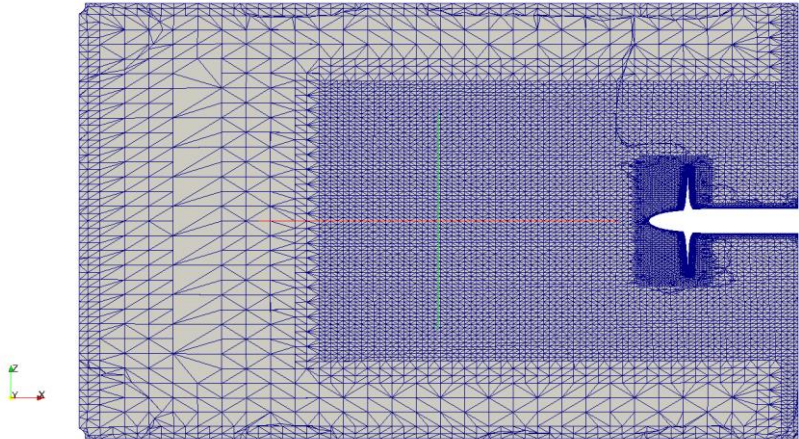
Figure 20. Definitive Mesh (plane XY)

ZOOM
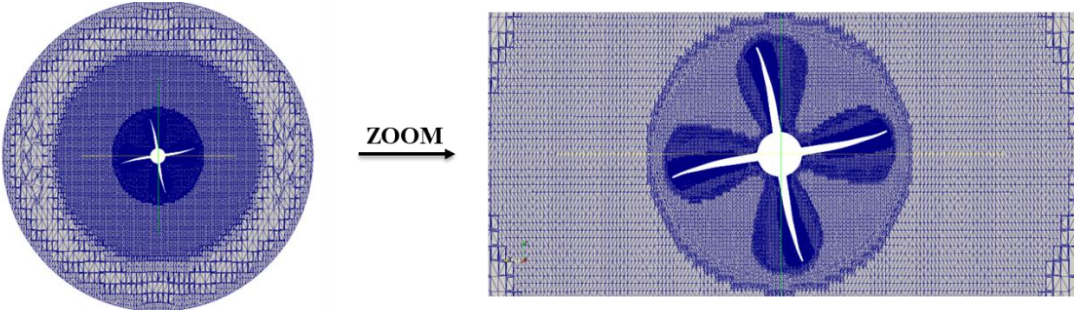
Figure 21. Definitive Mesh (plane YZ)

4.4.2. Meshing of Conventional Blade Profile.

Regarding the surface of the conventional propeller, an additional level of refinement has been applied where the cells deform and deviate from being regular hexahedrons, with the aim of improving mesh quality, as shown in Figure 22. Careful attention must be paid to the meshing of the surface edges, as they can affect the accuracy of the solution.
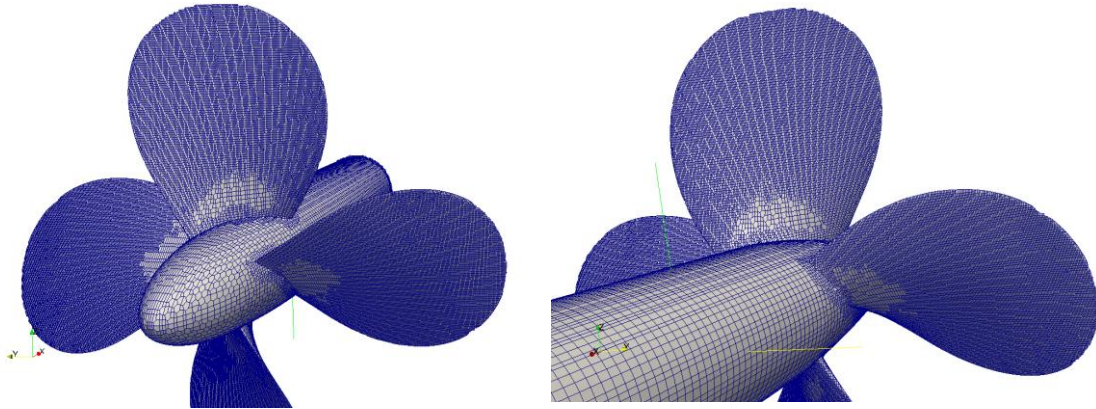
Figure 22. Conventional Blade Profile Mesh: pressure face (left) and suction face (right)

The edge size is 3% D_p in the most demanding areas and 6% in the remaining ones. Additionally, the descriptive parameters of the boundary layer are presented in Table 3, applying wall functions at $y^+ < 30$.

Table 3. Boundary Layer of the Conventional Blade Profile

BOUNDARY LAYER

Parameter	Value
Prism Layer Thickness	0.15%Dp - 0.20 [mm]
Aspect ratio	1.2
First Layer Thickness	0.1%Dp – 0.02 [mm]
Number of Sublayers	8

4.4.3. Meshing of High-Skew Angle Blade Profile

The geometry of the high-skew profile propeller is more complex and therefore requires a higher refinement. It is sufficient to increase by one additional level and have an edge size of 1.5% D_p in the most curved areas and 3% D_p, in the remaining regions, as shown in Figure 23.
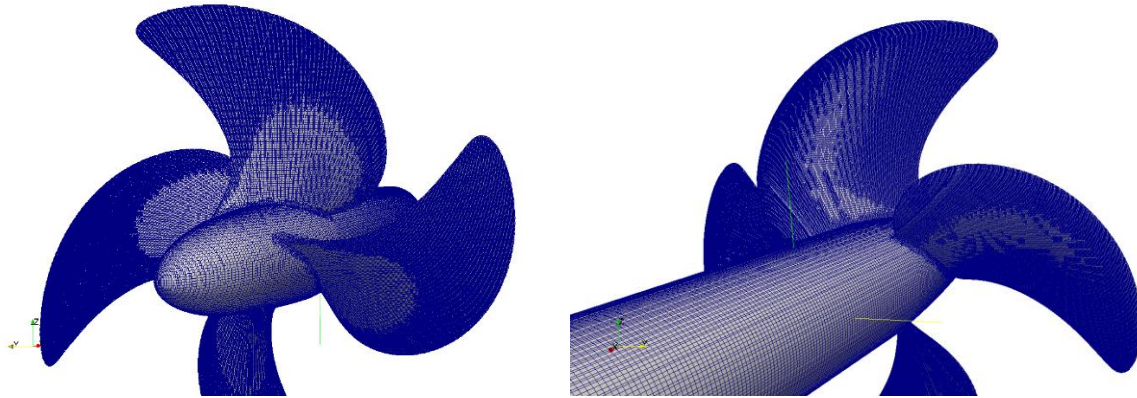
Figure 23. High-Skew Angle Blade Profile Mesh: pressure face (left) and suction face (right)

The descriptive parameters of the boundary layer are presented in Table 4, applying wall functions at $y^+ < 30$.

Table 4. Boundary Layer of the High-Skew Angle Blade Profile

BOUNDARY LAYER

Parameter	Value
Prism Layer Thickness	0.15%Dp - 0.20 [mm]
Aspect ratio	1.2
First Layer Thickness	0.1%Dp – 0.02 [mm]
Number of Sublayers	8

4.4.4. Quality of Resulting Mesh

The mesh quality of the mesh is an extremely important characteristic of a simulation, as it is directly related to the convergence and accuracy of the solution. No matter how fine the mesh is, if the elements initially defined as hexahedrons deviate from that shape, the quality is poor and the results obtained will not be as expected. It is even possible that the simulation could fail due to inconsistencies, known as *floating points*.

Below are the key parameters that indicate the mesh quality for both propellers, including the total number of cells for each domain.

Table 5. Quality of the Resulting Mesh: Conventional Blade Profile

Parameter	Value
Max. Cell Openness	3.339e-16 [OK]
Max. Aspect Ratio	31.109 [OK]
Max. Mesh Non-Orthogonality	66.475 [OK]
Max. Skewness	4.893 [OK]
Number of Cells	**583459**

Table 6. Quality of the Resulting Mesh: High-Skew Angle Blade Profile

Parameter	Value
Max. Cell Openness	3.368e-16 [OK]
Max. Aspect Ratio	31.134 [OK]
Max. Mesh Non-Orthogonality	67.961 [OK]
Max. Skewness	4.921[OK]
Number of Cells	**673048**

4.5. Definition of Cell Zone

Finally, as far as the simulation domain is concerned, a new cell zone, called *CVZone*, is defined in order to collect the desired information of interest inside it. In this case, it is a geometry that covers the size of a propeller blade and is intended to collect the volume of water in each of the cells. As shown in the Figure 24 for the conventional profile propeller, this area is located inside *innerCylinder* so that *CVZone* will also rotate at the same speed.
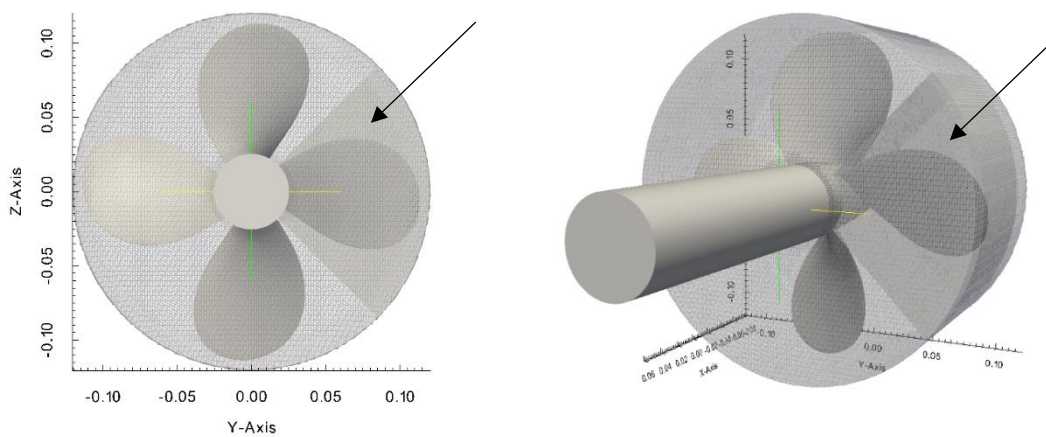
Figure 24. Definition of CVZone for conventional blade profile

It is important to emphasise that this defined area around the blade does not increase the number of cells, but just identifies the cells' identity inside it. In this way, the cavitation volume is captured much better and the post-processing is more coherent, because the information of what happens in *innerCylinder* includes the volume that two blades can have at the same time.

Similarly, information is collected from one of the high-skew profile blade, as shown in Figure 25, using a modified *CVZone* cell zone in a way that fits the blade and does not collect phase-change information from the immediately following ones, since it will distort the data.
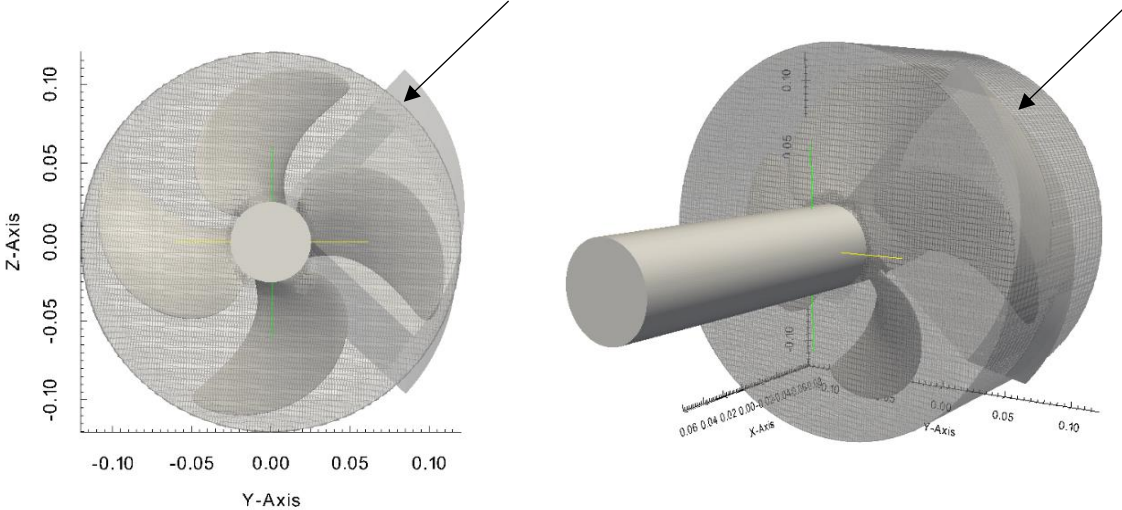
Figure 25. Definition of CVZone for high-skew angle blade profile

4.6. Physical Parameters

The simulations are conducted at a temperature of 20 ºC. The physical parameters of water, both in liquid and vapour phase, are collected in Table 7, as defined in [12].

Table 7. Physical Parameters of the Fluids (liquid and vapour)

Parameter	Value
T [˚ C]	20
ρ_{water} [kg/m^3]	998
υ_{water} [m^2/s]	1.01 x 10^{-6}
p_{vapour} [Pa]	2.337 x 10^3
ρ_{vapour} [kg/m^3]	0.017
μ_{vapour} [Ns/m^3]	1.02 x 10^{-5}

The cavitation number based on the propeller rotational speed is used here to define the pressure conditions (p_∞), at a constant revolution rate of 30.5 rps and free-stream velocity of 6.22 m/s. Different operating conditions, shown in Table 8, are evaluated in order to investigate the effect of blade loading and field pressure on cavitation.

Table 8. Pressure - σ_n Values

σ_n	p_∞ [Pa]
1.5	38.301
2	50.289
2.5	62.278

The simulations for both conventional and high-skew blades are performed at an advance coefficient **J = 0.897**,

$$J = \frac{V_A}{n\,D_p} \tag{26}$$

where V_A is the velocity that arrives to the propeller disk in [m/s], **n** is the revolution rate in [rps] and D_P is the propeller diameter in [m].

4.7. Boundary Conditions

As stated in previous sections, the simulation is solved using the Reynolds-Averaged Navier-Stokes equations (RANS), which govern the velocity and pressure of fluid flow, and additionally, the k-ε turbulence model.

In flow driven analyses, the boundary condition combination for the inlet and outlet region is defined as inlet for the wake field and outlet for the pressure, [32]. In OpenFOAM, the static pressure is represented by *p*, or *p_rgh* when subtracting the pressure due to the liquid column. In the present case the reference height (h) can be considered as 0, such that p_∞ is directly defined as an outlet boundary condition. The velocity and pressure boundary conditions are as follows in Table 9 and Table 10.

Table 9. Boundary Conditions of Velocity Field

Boundary	Type	Velocity
Inlet	Patch	timeVaryingMappedFixedValue
Outlet	Patch	pressureInletOutletVelocity
OuterCylinder	Wall	noSlip
Propeller	Wall	movingWallVelocity

Table 10. Boundary Condition of Pressure Field

Boundary	Type	Pressure
Inlet	Patch	fixedFluxPressure
Outlet	Patch	totalPressure
OuterCylinder	Wall	inletOutlet
Propeller	Wall	FixedFluxPressure

Finally, the boundary conditions for turbulent kinetic energy per unit mass (k), the turbulent dissipation rate (ε) and the kinematic viscosity (ν) are collected in Table 11.

- Turbulent kinetic energy per unit mass (k). It represents the energy associated with the turbulent fluctuations of velocity in the flow.
- Turbulent dissipation rate (ε). It represents the rate at which turbulent energy is dissipated into internal energy due to viscous effects.
- Kinematic viscosity (ν). It characterizes how easily the fluid flows in response to a shearing force.

Table 11. Boundary Conditions of Turbulence Parameters

Boundary	ε	nut	k
Inlet	*fixedValue*	*calculated*	*fixedValue*
Outlet	*inletOutlet*	*calculated*	*inletOutlet*
OuterCylinder	*inletOutlet*	*inletOutlet*	*inletOutlet*
Propeller	*epsilonWallFunction*	*nutWallFunction*	*kqRWallFunction*

Once the simulation is launched, the flow development around the cylinder and along the domain are observed, by performing cuts according to the XZ and YZ planes. The velocity gradient is smooth and the flow deflects to the left due to the momentum generated by the propeller rotation.
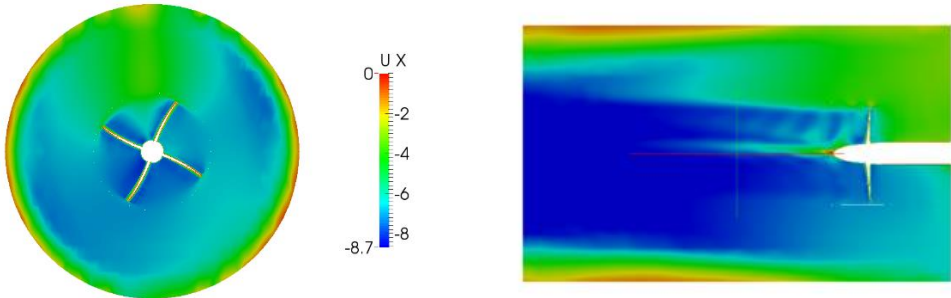
Figure 26. Resultant Flow: plane XY (left) and plane YZ (right)

4.8. Courant Number

The parameter that controls the simulation and is directly related to the mesh size is the Courant number (*Co*). It is applied in the solution of partial differential equations, to be more precise, including advection and time-dependent problems, and for explicit integration schemes, so that it requires to be bounded by certain constant in order to keep stability (not to diverge), [17].

It provides a measure of the rate at which information is transported under the influence of a flux field, which refers to the distribution and flow of a fluid quantity (mass, momentum or energy) and quantifies how much of that quantity passes through a closed surface over time.

The Courant number is the quotient of the time interval and the residence time in a finite volume, as defined in Equation (27) , so that it marks the upper limit of the internal time interval used by certain algorithms, i.e. is a limiting factor for the performance of numerical schemes.

$$Co = \frac{U \, \Delta t}{\Delta x} \qquad (27)$$

It can be explained graphically as shown in Figure 27. If the Courant number is lower than 1, fluid particles move from one cell to another within one time step at most. If it is higher than 1 a fluid particle moves through two or more cells at each time step and this can affect convergence negatively, especially in transient simulations. For this reason, a value of **0.5** is usually set.
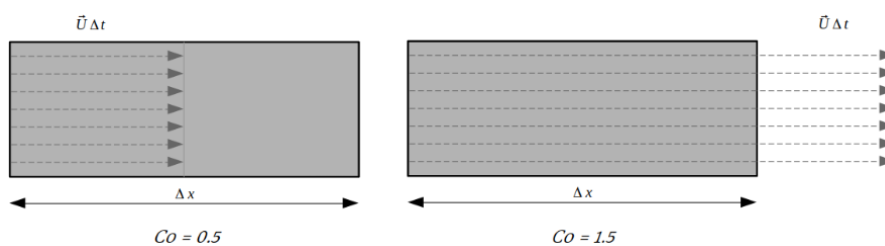
Figure 27. Explanation of Courant Number Concept in Computational Fluid Dynamics (CFD), [17]

The time step (Δt) of the simulations is also adjusted, in such a way that it is directly related to that angular step ($\Delta \theta$) that the sweep ensures good accuracy in the results. A maximum time step not exceeding 1° is set and, considering the revolution rate of the propeller, it is equivalent to $1 \cdot 10^{-4}$ seconds.

5. ANALYSIS OF THE RESULTS

5.1. Cavitating Case Study

This section includes the post-processing of the simulations, covering the analysis of the obtained data: cavitation volume and pressure curves, graphical representation of cavitation, signal filtering and Fourier transform. All of this is carried out for both propellers, with the aim of analysing the information in a standardized manner and avoiding data deviations that could lead to errors.

5.1.1. Conventional Profile Propeller Blade

First the conventional profile propeller blade is simulated. Prior to the analysis of radiated noise, it is observed that the simulation requires a specific time to stabilize the pressure field and initiate cavitation, when $p < p_v = 2339$ Pa. It approximately takes 0.038 seconds, which is 420º.
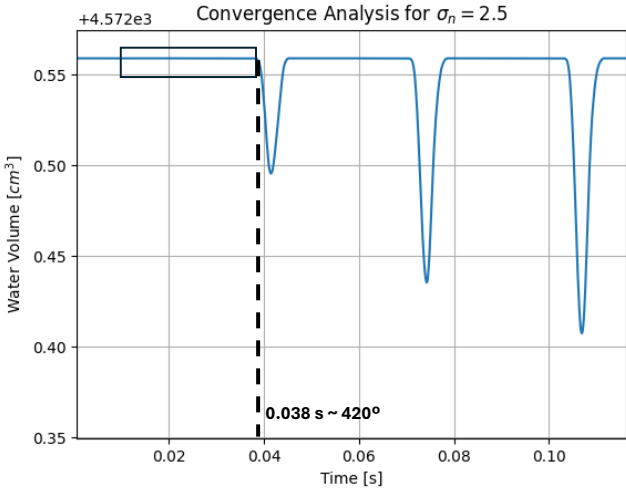
Figure 28. Time required to initiate cavitation

Another aspect is the increase in cavitation volume with increasing simulation time and, therefore, it is necessary to observe the convergence behaviour to select the range with the highest volume. It is decided to analyse what occurs around 0.82 seconds, when cavitation is fully developed.
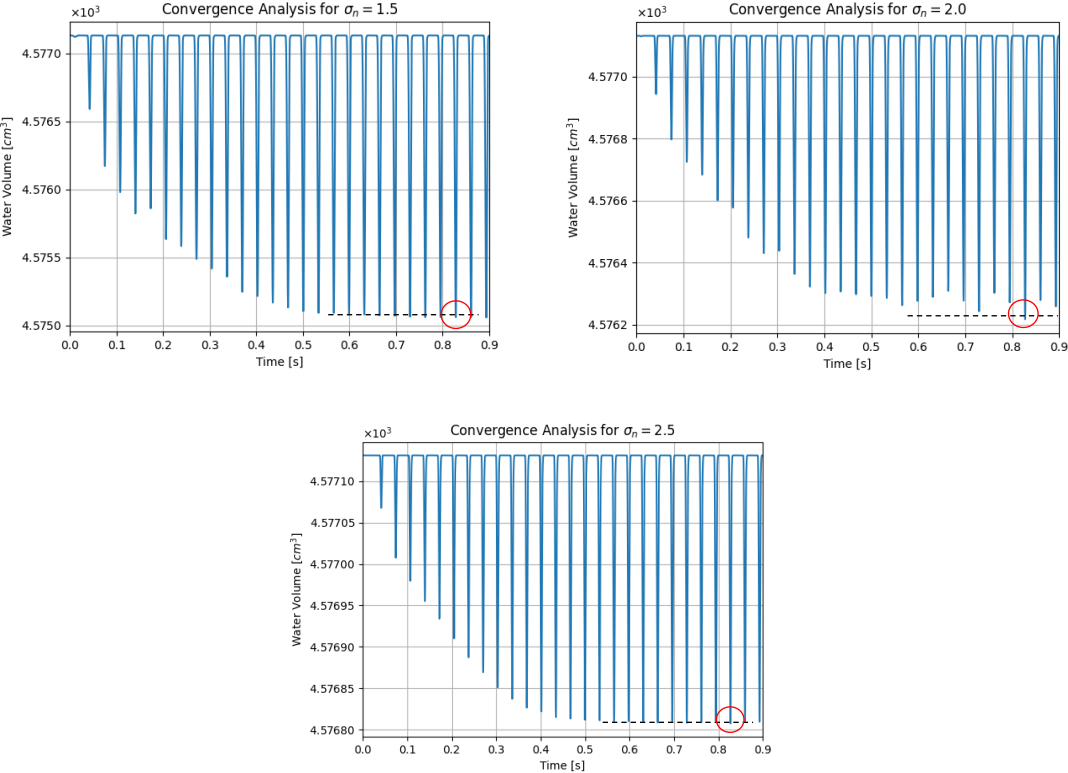
Figure 29. Development of the Cavitation Volume: Convergence

Cavitation occurs first in the suction area of the propeller blade, as this is the area of lowest pressure. Figure 30 shows how the cavitation volume varies according to the relative position of the propeller blade, particularly at $\sigma_n = 2.5$ (sequence starting from top left to lower right).

It is observed that in the operating regime selected for the analysis, cavitation occurs only on one blade, although it can potentially occur simultaneously on more than one blade. This will depend on the inlet wake field profile, which will define the pressure field on the propeller disk. In this case, since the profile is very thin, cavitation occurs only on the upper blade, reaching its maximum value at 90º, considering that the blade under analysis is the one situated in the right-hand side.
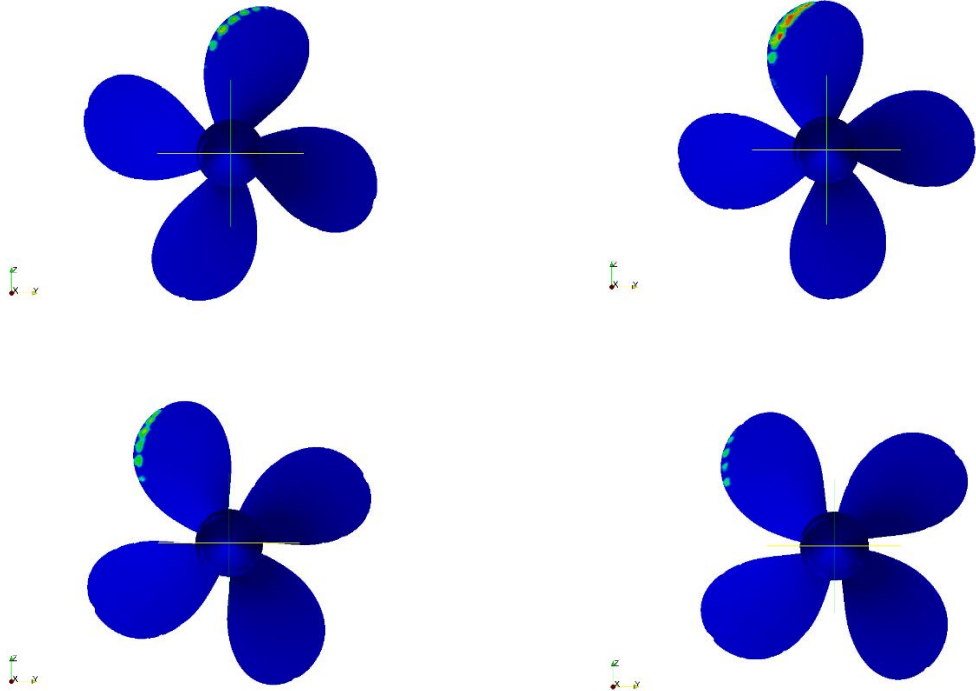
Figure 30. Evolution of the Cavitation Volume at $\sigma_n = 2.5$

45

Transferring the volume into the sound pressure by double differentiation, as explained in section 2.1. **Underwater Radiated Noise**, and applying monopole law, described by Equation (8), the pressure signal is obtained noisy, as expected. Pressure spikes can be observed where the curvature of the function changes abruptly, i.e. cavity growth, highest volume point and mainly cavity collapse stretch. Following monopole equation, the longer the distance from source to observation point (r), the lower the pressure and therefore the received noise. It is therefore convenient to simply represent the volume acceleration, as it is directly proportional to the magnitude of the pressure, i.e. assuming

$$\frac{\rho}{4\,\pi\,r} \sim 1$$

From Figure 31 to Figure 33, volumes and accelerations for the different cavitation numbers are shown.
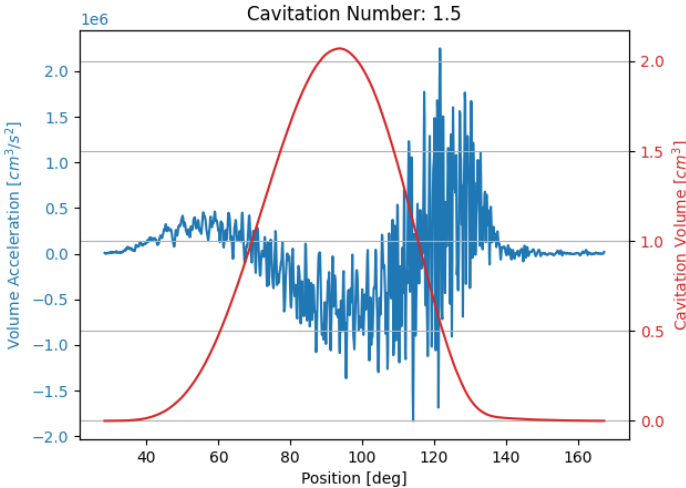
Figure 31. Cavitation Volume and Pressure Signal (i.t.o. Acceleration) - σ_n=1.5
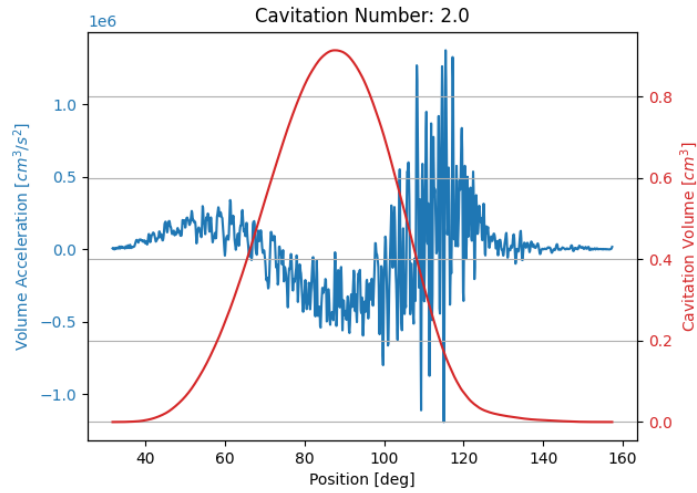
Figure 32. Cavitation Volume and Pressure Signal (i.t.o. Acceleration) - σ$_n$=2.0
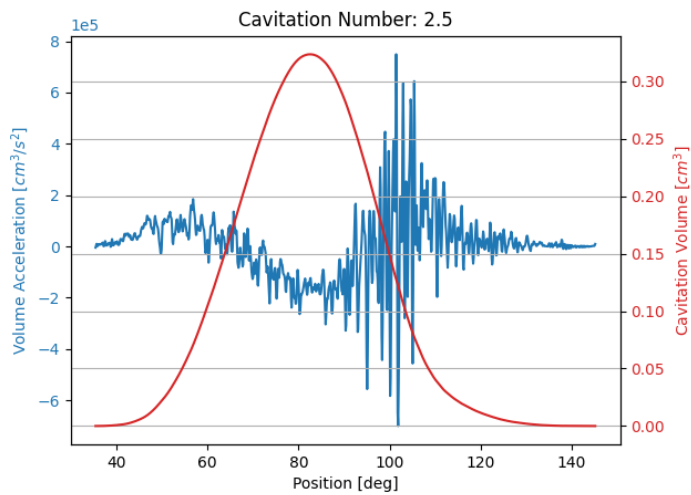
Figure 33. Cavitation Volume and Pressure Signal (i.t.o. Acceleration) - σ$_n$=2.5

The maximum values of cavitation volume are collected in Table 12, increasing as the cavitation number decreases.

Table 12. Maximum Volume of Sheet Cavitation Bubble

σ$_n$	p$_\infty$ [Pa]	V [cm^3]
1.5	38.301	2.071
2	50.289	0.914
2.5	62.278	0.324

It is important to note how the pressure (p_∞), through σ_n, affects not only the amount of cavitation but also the smoothness of transitions, with wider curves at higher cavitation numbers. In Figure 34, that volume is graphically represented along with values from Table 13, where black curve represents $\sigma_n = 1.5$, red curve represents $\sigma_n = 2.0$ and blue curve represents $\sigma_n = 2.5$.

Table 13. Evolution of Sheet Cavitation Bubble

σ_n	p_∞ [Pa]	Growth	Collapse
1.5	38.301	28.19º	167.42º
2	50.289	31.70º	157.43º
2.5	62.278	35.33º	145.24º
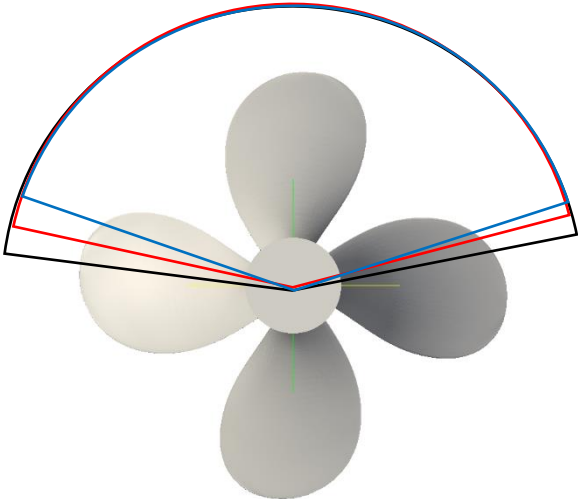
Figure 34. Range of Sheet Cavitation Volume for several σ_n

In this way, by transferring the pressure signals to the frequency domain by applying the Fourier Transform, the radiated noise spectrum for each of the cavitation numbers is obtained. From Figure 35 to Figure 37, water-borne spectrums for the different cavitation numbers are shown.
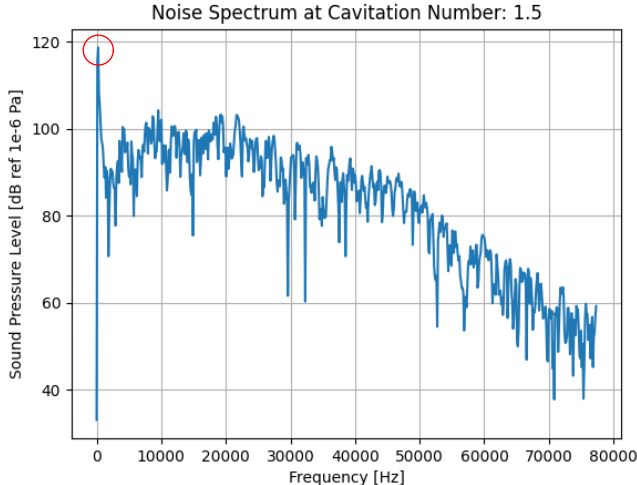
Figure 35. Noise Spectrum of the Unfiltered Pressure Signal - σ_n=1.5
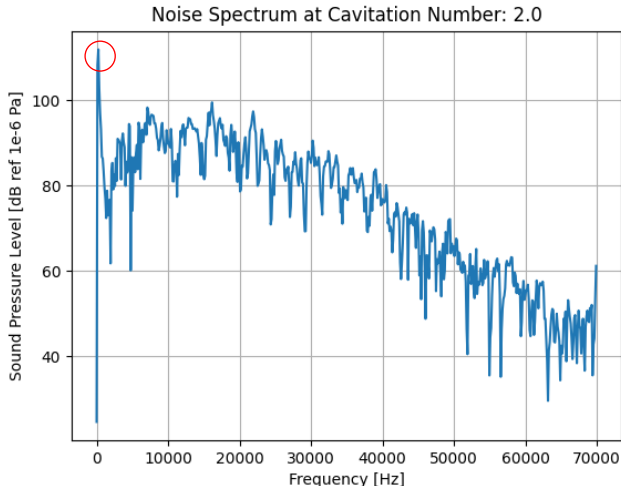
Figure 36. Noise Spectrum of the Unfiltered Pressure Signal - σ_n=2.0
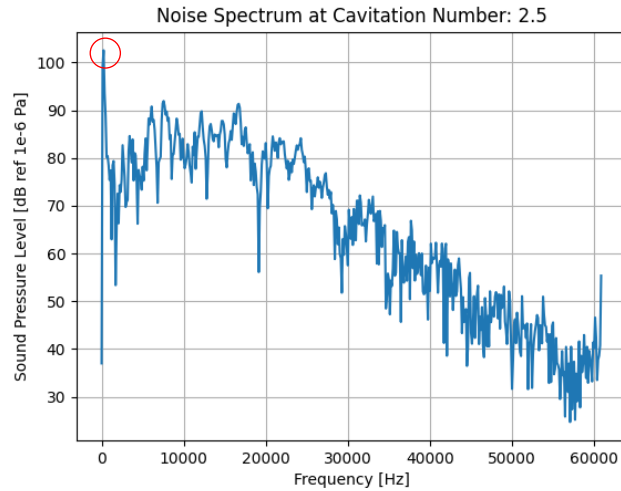
Figure 37. Noise Spectrum of the Unfiltered Pressure Signal - σ_n=2.5

When studying radiated noise in the frequency domain it is important to consider the numerical fluctuations that represent high frequency noise, which in this case we want to avoid. This is why the pressure signal must be smoothed before calculating the FFT, which will not modify the low frequency component in any way. In consideration of the above, the smoothed pressure signals are presented from Figure 38 to Figure 40.
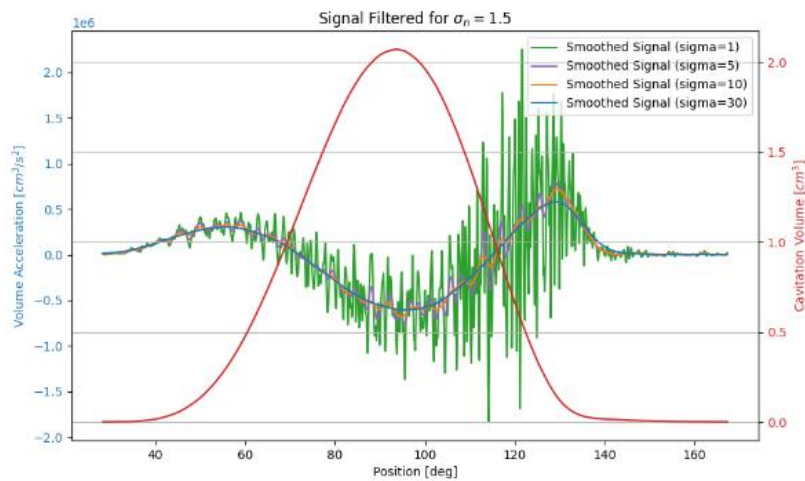
Figure 38. Pressure Signal Filtered for Low-Frequency - σ_n=1.5
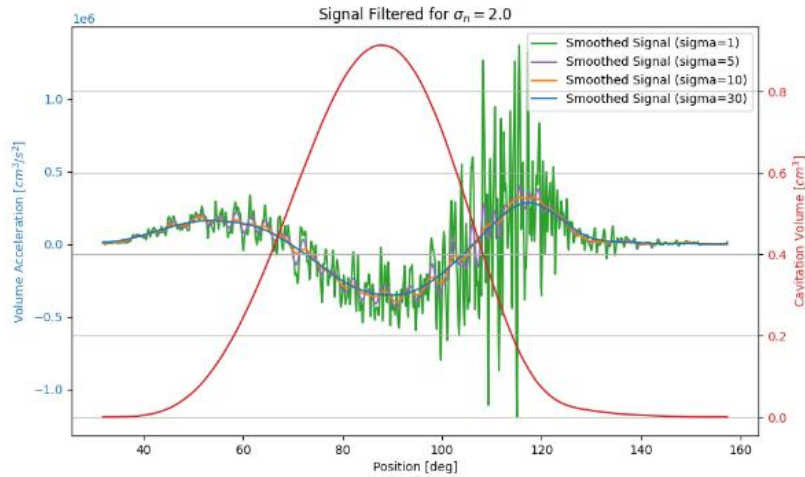
Figure 39. Pressure Signal Filtered for Low-Frequency - σ_n=2.0
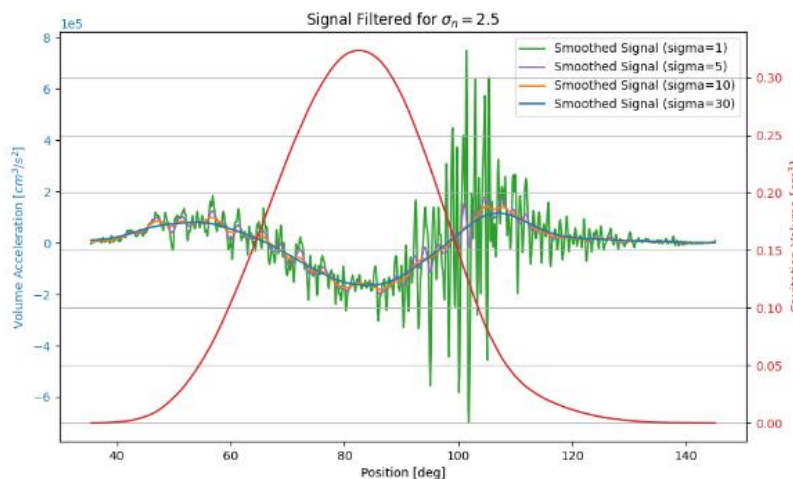
Figure 40. Pressure Signal Filtered for Low-Frequency - σ_n=2.5

Applying the Fast Fourier Transform (FFT) to the smoothed pressure signal, the sound pressure level in [dB] is obtained in the frequency domain and it is observed that the radiated pressure excitation arising from a cavitating marine propeller operating behind a ship principally comprises **two** characteristic types, that can be seen on either side of 1000 Hz. The first is the **blade rate harmonics**, due to the pressure signal is not a perfect sinus function, whose amplitudes should decay monotonically. The second is the **broadband** spectrum with some additional tonal noise of higher frequency, which disappear when the pressure is smoothed (orange curve).

Figure 41 to Figure 46 compares the values in [dB] of the spectrum from the original pressure signal (blue curve) and the filtered pressure (orange curve), where the peaks align with the blade frequency harmonics (revolution rate time the number of blades). As can be seen in Figure 6. Noise Spectrum of a Container Ship, furnished by DWShipConsult, there is a maximum at 40 or 50 Hz, i.e. at around 5th harmonic of blade rate. In the present case, a peak at low frequency can be observed, in particular at the 2nd harmonic of blade rate, i.e. 244 Hz since blade rate is 122 Hz.

Figure 41. Noise Spectrum of the Filtered Pressure Signal - σ_n=1.5
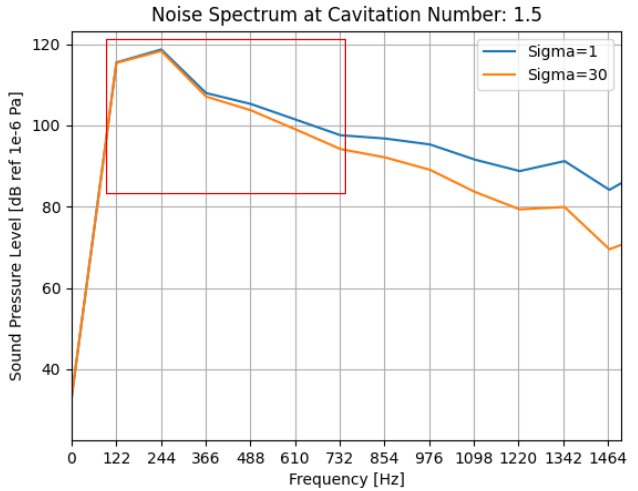
Figure 42. Noise Spectrum of the Filtered Pressure Signal - σ_n=1.5 – Zoom at Low Frequencies
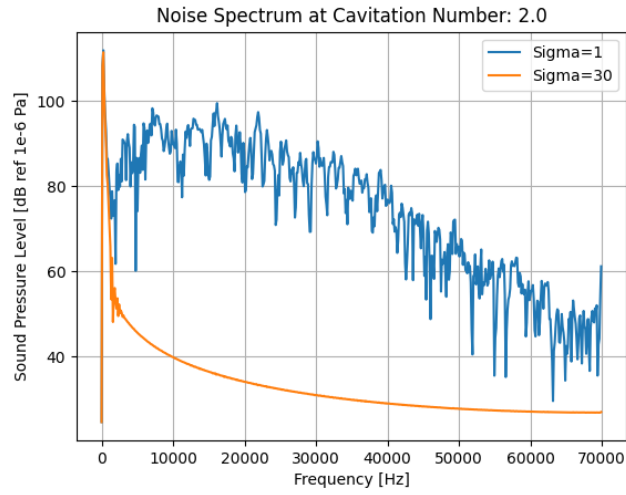
Figure 43. Noise Spectrum of the Filtered Pressure Signal - σ_n=2.0
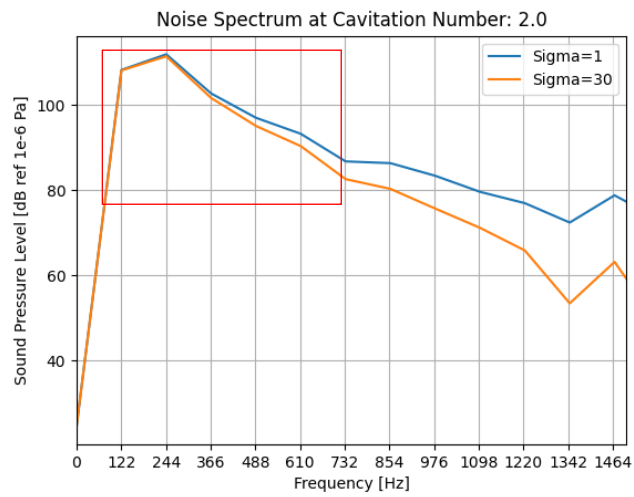
Figure 44. Noise Spectrum of the Filtered Pressure Signal - σ_n=2.0 – Zoom at Low Frequencies
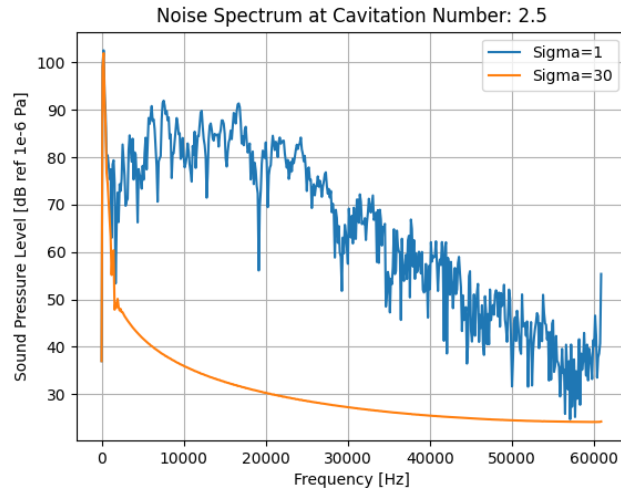
Figure 45. Noise Spectrum of the Filtered Pressure Signal - σ_n=2.5
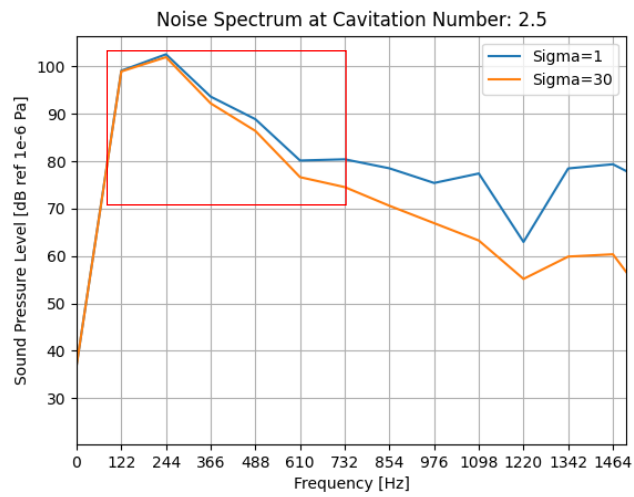
Figure 46. Noise Spectrum of the Filtered Pressure Signal - σ_n=2.5 – Zoom at Low Frequencies

Noise spectrums usually indicate that the first two harmonics are reasonably close to each other in terms of amplitude, and the discrepancy increases at higher harmonics. The number of harmonics, for sheet cavitation on the blade, is strongly related to the gradient of the wake. In the present case, the first 5 harmonics are very close to each other (from 122 Hz to 610 Hz). Subsequently, the radiated noise levels in [dB] are collected in Table 14 at various cavitation numbers, which increase with the amount of cavitation that occurs.

Table 14. Noise Levels in [dB] for several σ_n

Frequency [Hz]	URN [dB] at $\sigma_N = 1.5$	URN [dB] at $\sigma_N = 2.0$	URN [dB] at $\sigma_N = 2.5$
122	115	108	99
244	118	111	101
366	106	100	90
488	101	92	82
610	95	86	70

The three evaluated conditions are graphically represented in Figure 47.
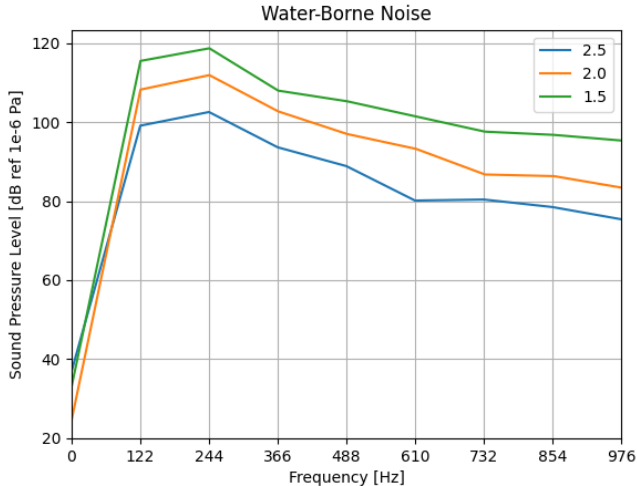
Figure 47. Comparison of Noise Levels in [dB] for several σ_n

5.1.2. High-skew Angle Profile Propeller Blade

Next, the procedure explained so far in this section is carried out for the high-skew profile propeller blade. Again, the time required to stabilize the pressure field and develop cavitation, as well as the convergence of the cavitation volume are observed. The same point is selected as for the conventional propeller, i.e. **0.82 seconds** of simulation time.
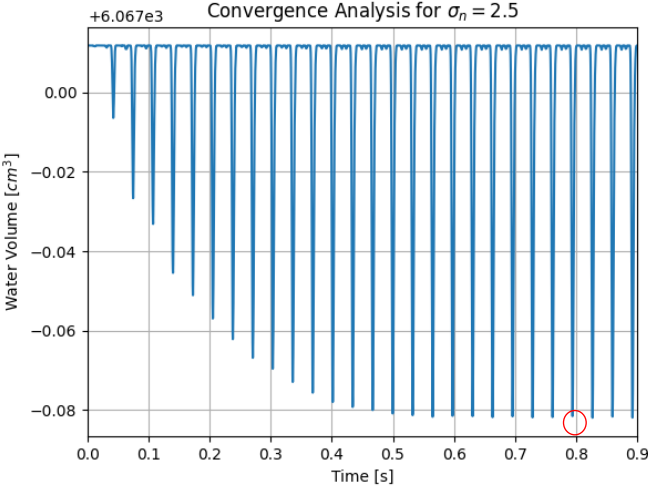
Figure 48. Development of the Cavitation Volume: Convergence

This propeller has been simulated at a single cavitation number, as its effect on radiated noise has already been demonstrated for the conventional propeller. Figure 49 shows the evolution of the cavitation bubble on the suction side of the blade, at $\sigma_n = 2.5$ (sequence starting from top left to lower right).
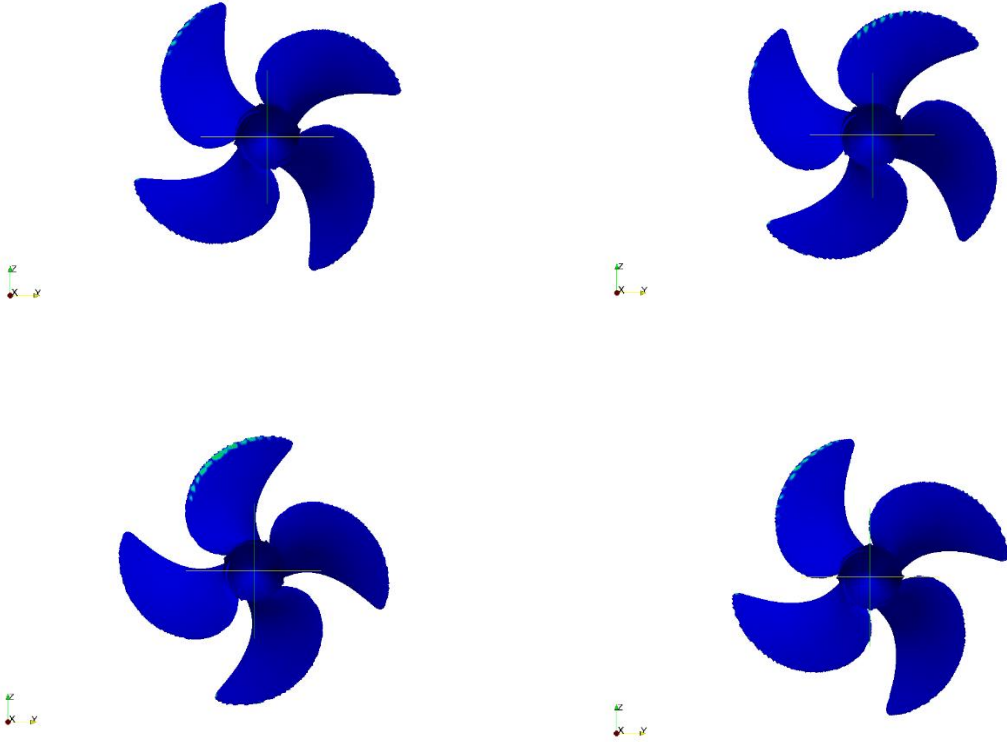
Figure 49. Evolution of the Cavitation Volume at $\sigma_n = 2.5$

By applying the monopole equation, the pressure signal is obtained less noisy, as expected. In terms of the shape of the curve, the final section is much smoother, which means a reduction in pressure variation.
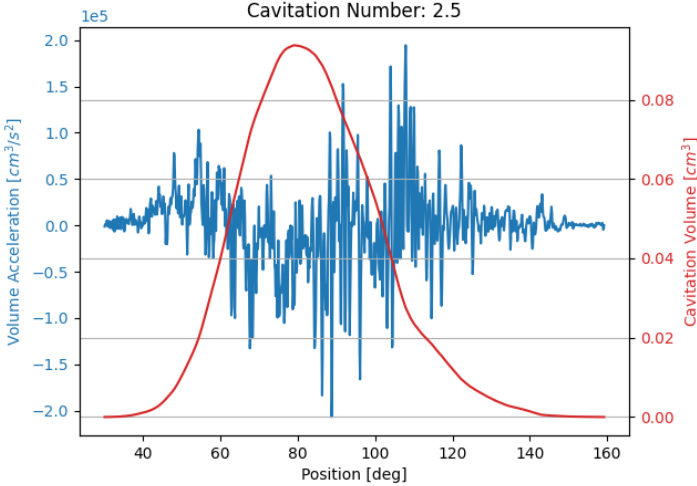
Figure 50. Cavitation Volume and Pressure Signal (in terms of Acceleration of Cavitation Volume)

In Table 15, the main characteristics of the sheet cavitation volume can be read. In conclusion, it is primarily noted that the cavitation range is greater than in the previous case. It starts and ends at lower positions in the propeller disk, which translated to a larger cavitation evolution angle.

Table 15. Sheet Cavitation Bubble Volume and Evolution

Growth	Collapse	V [cm^3]
30.03˚	159.24˚	0.094

When moving to the frequency domain, it is observed again that it is necessary to filter the pressure signal to remove high-frequency components, as shown in Figure 51.
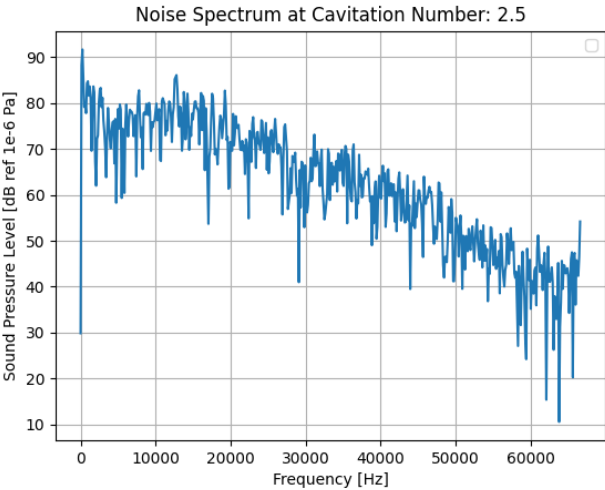
Figure 51. Noise Spectrum of the Unfiltered Pressure Signal

The pressure signal is smoothed to eliminate high-frequency components, and similarly, the resulting spectrum is obtained as desired. When zoom is performed, lower noise levels in [dB] are observed in Figure 52.
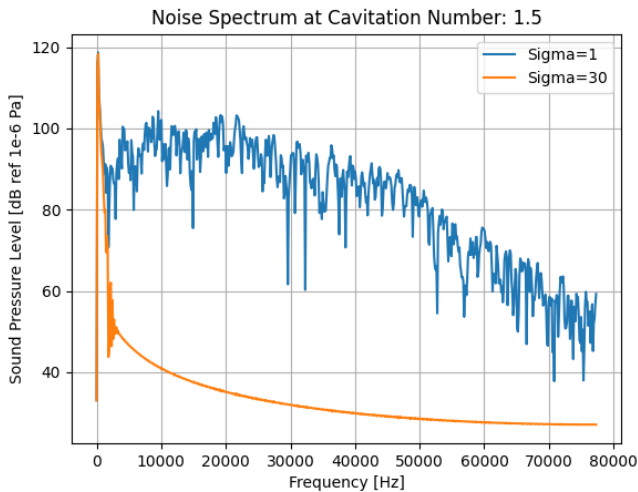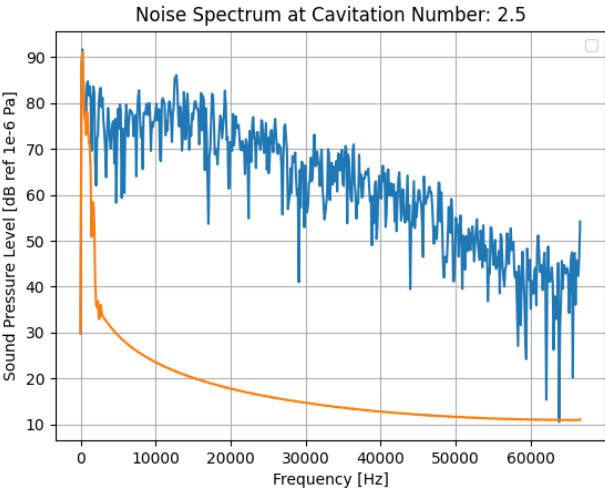

Figure 52. Noise Spectrum of the Filtered Pressure Signal
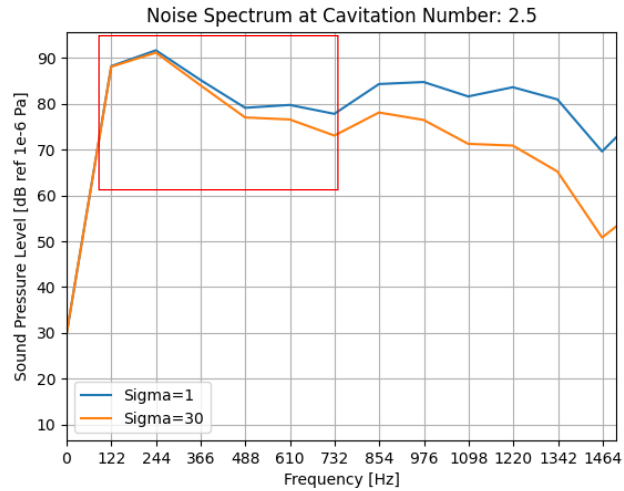
Figure 53. Noise Spectrum of the Filtered Pressure Signal - Zoom at Low Frequencies

5.1.3. Comparison of Geometries in Radiated Noise

The results obtained for comparison include the shape of the cavitation curve, the total volume of cavitation and the noise levels in the propeller harmonics, at cavitation number of 2.5. The shape of the curve representing the collapse of the cavitation bubble is wider and smoother when using high-skew blade profiles as observed in Figure 54, meaning that cavitation covers a larger time range, resulting in significantly reduced noise levels. The cavitation volume is notably reduced, by a 73%. The vertical right-hand axis, in Figure 54, represents the values for the conventional propeller blade while the left-hand axis for the high-skew propeller blade.
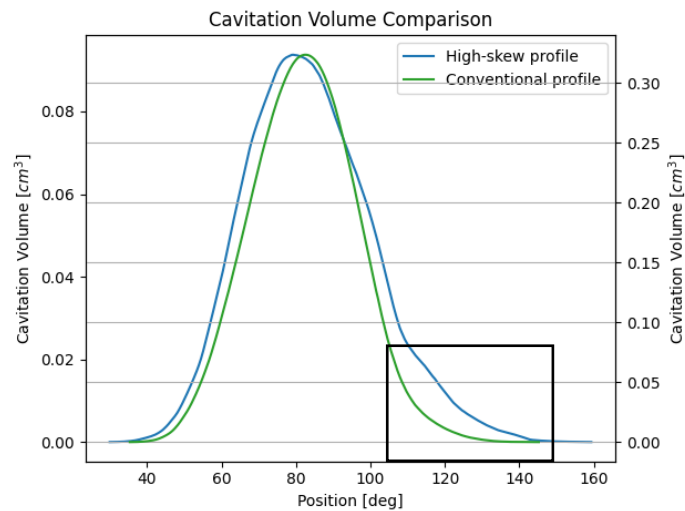
Figure 54. Comparison of Cavitation Volume: Conventional and High-Skew Angle Blade Profile

When comparing the radiated noise levels, it is much more convenient to do so in the first 3 harmonics. Thus, both spectrums plotted on the same graph are obtained from the corresponding pressure curves, already appropriately smoothed.
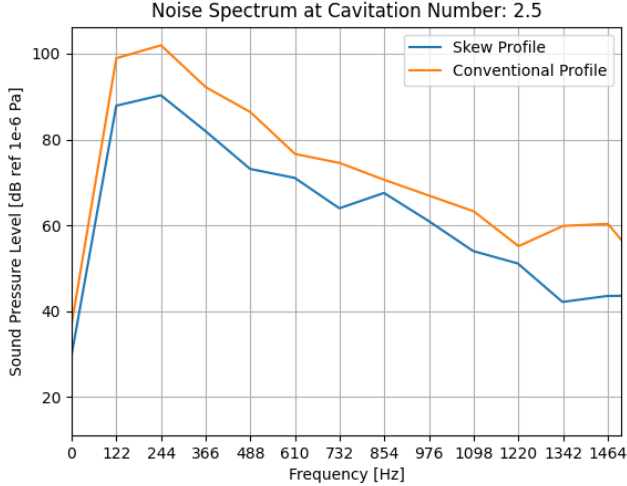
Figure 55. Comparison of Noise Spectrum: Conventional and High-Skew Angle Blade Profile

The corresponding values for the first 3 harmonics are compared in Table 16, where an average of 12 dB noise reduction is achieved.

Table 16. Noise Level Reduction

Frequency [Hz]	URN [dB] reduction
122	13
244	12
366	11

5.2. Non-Cavitating Case Study

The solver *pimpleFoam* was introduced earlier because it will be used to calculate the effective disk area of the propeller in the same conditions as above but not modelling cavitation (single-phase flow), paying attention to the pressure field and reinforcing the idea that the results obtained should not differ significantly from those obtained with phase change.

This study could in turn be contrasted with a potential flow software obtaining the propeller velocity and pressure field, by reconstructing the volumetric face-flux field (*phi*). Obviously, it is a way to save computational cost. The images shown in Figure 56 for the conventional blade profile, and in Figure 57, for the high-skew blade profile, at σ_n = 2.5, show the pressure distribution that matches with the cavitation bubble evolution profile, obtained with RANS model without considering phase change (sequence starting from top left to lower right).
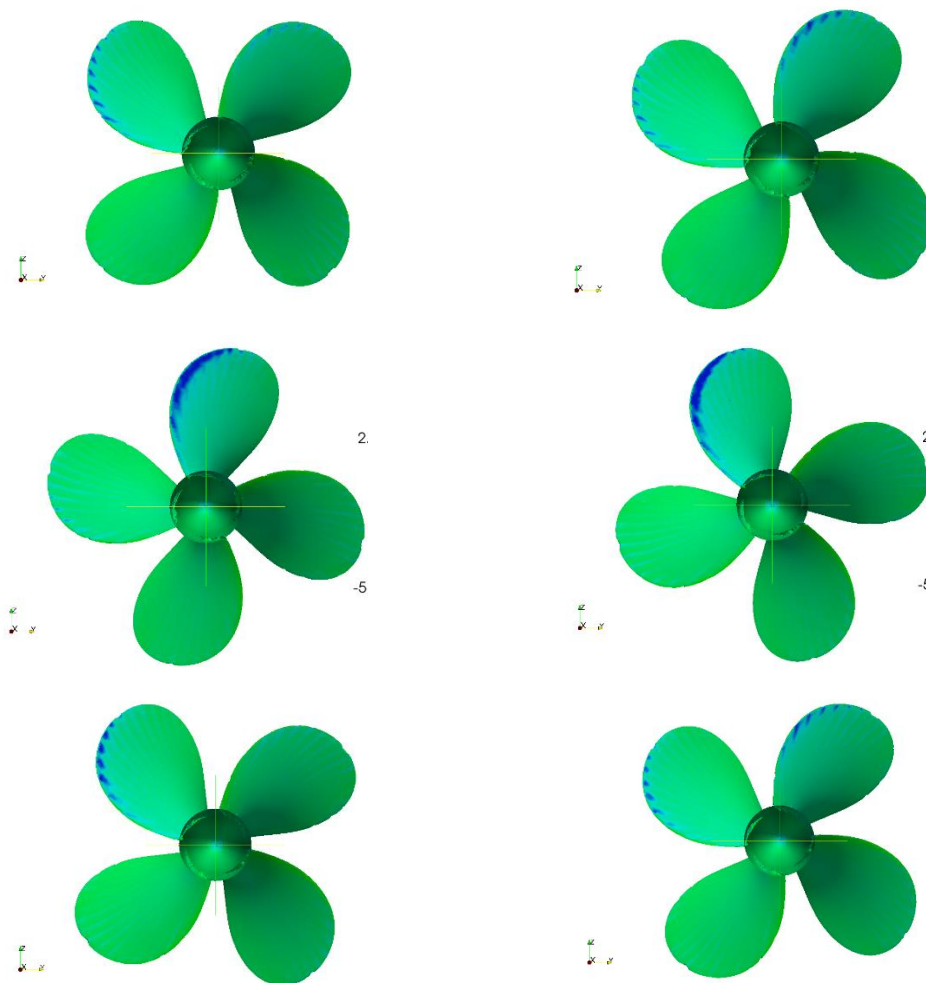
Figure 56. Evolution of the Pressure Field in the Suction Side: Conventional Blade Profile

Figure 57. Evolution of the Pressure Field in the Suction Side: High-Skew Angle Blade Profile

Therefore, as the area-time function of the low-pressure region appears to look similar to the volume-time function with the cavitation bubble modelled it is justified to expect that this much simpler calculation can be used to optimize a blade shape in routine projects. The findings can then be verified by a complete RANS calculation modelling cavitation. This needs further investigations.

6. CONCLUSIONS

A numerical study has been carried out to predict and compare noise characteristics of a conventional and high-skew blade profile, based on the 4-bladed INSEAN E779A propeller, subjected to an imposed wake, by using a Reynolds Average Navier Stokes (RANS) method. The conclusions drawn from the study are as follows:

- A reduction of the noise level in 12 dB was observed by varying the skew angle. For merchant ships, where the inlet flow to the propeller is characterized by a low pressure in the upper part, it has been shown that geometries with a high skew angle reduce the noise radiated by sheet cavitation.

- Noise reduction can be reduced as well by using two shaft lines, so that the propeller revolution rate is reduced and thus the cavitation number increases.

- Noise can be estimated as well through the variation of the blade area with $p < p_{vapour}$, since pressure development profiles are similar to those of sheet cavitation. Then potential solvers can be used to get an idea of the noise that might radiate from a flow around an object. While this approach is not entirely accurate, it is performed at a low computational cost.

An important aspect that requires explanation is the verification of the simulations. There are no available data due to both the confidentiality surrounding noise issues and the fact that the operating conditions of the propeller differ from what might be encountered, owing to the specific inflow profile and the rotational speed of the propeller. Both propellers have been simulated under the same conditions, and what matters is the comparison between them. Observing a reduction in decibels (12 dB), which would result in a substantial reduction in global underwater noise, is a good basis for further work along this line.

7. FUTURE LINES OF WORK

Despite the complexity of the work conducted, there are various paths open for future research, that could contribute significant value to the topic of radiated noise from marine propellers.

- Inflow profiles resulting from ship hulls. Studying the impact of different wake-fields on the radiated noise from a propeller.
- Implementing a potential flow model to determine the area of the blade below vapour pressure and comparing its variation profile with the cavitation volume curve.

ACKNOWLEDGEMENTS

REFERENCES

[1] Artur K. Lidtke, Stephen R. Turnock and Victor F. Humphrey, 2016. Characterization of sheet cavity noise of a hydrofoil using the Ffowcs Williams-Hawkings acoustic analogy. *ScienceDirect Computer and Fluids*, Volume 130, Pages 8-23.

[2] C. Testa, S. Ianniello and F. Salvatore, 2018. A Ffowcs Williams and Hawkings formulation for hydroacoustic analysis of propeller sheet cavitation. *Journal of Sound and Vibration*, Volume 413, Pages 421-441.

[3] Francesco Salvatore, Heinrich Streckwall and Tom van Terwisga, 2009. Propeller cavitation modelling by CFD – Results from the VIRTUE 2008 Rome Workshop. *First International Symposium on Marine Propulsors*, Trondheim, Norway.

[4] Leonie S. Föhring, Peter Møller Juhl and Dietrich Wittekind, 2023. Experimental parameters influencing the cavitation noise of an oscillating NACA0015 hydrofoil. *Journal of Marine Science and Engineering*, Volume 11 (issue 10: Cavitation Dynamics and Underwater Radiated Noise in Ocean Engineering).

[5] Leonie S. Föhring, Peter Møller Juhl and Dietrich Wittekind, 2022. On the influence of cavitation volume variations on propeller broadband noise. *Journal of Marine Science and Engineering*, Volume 10 (issue 12: Assessing the Pressure of Underwater Anthropogenic Noise from Impulsive and Continuous Sound Sources).

[6] Leonie S. Föhring, Peter Møller Juhl and Dietrich Wittekind, 2022. Cavitation volume behaviour derived from full-scale pressure fluctuations. Ships and Offshore Structures, Volume 18, Pages 541-549.

[7] Alex Zinoviev, 2002. Application of Ffowcs Williams and Hawkings equation to sound radiation by vibrating solid objects in a viscous fluid: inconsistencies and the correct solution. *Innovation in Acoustics and Vibration, Annual Conference of the Australian Acoustical Society*, Adelaide, Australia.

[8] S. Ianniello and C. Testa, 2019. An overwiew on the use of the Ffowcs Williams and Hawkings equation for the hydroacoustic analysis of marine propellers. *VII International Conference on Computational Methods in Marine Engineering, MARINE 2019*.

[9] Eirik B. Njaastad, Olav Egeland and Sverre Steen, 2022. Identification of the geometric design parameters of propeller blades from 3D scanning. *Journal of Marine Science and Technology*, Volume 27, Pages 887-906.

[10] Stefano Gaggero and Diego Villa, 2018. Cavitating propeller performance in inclined shaft conditions with OpenFOAM: PTTC 2015 test case. *Journal of Marine Science and Application*, Volume 17, Pages 1-20.

[11] Daniel A. Russell, Joseph P. Titlow and Ya-Juan Bemmen, 1998. Acoustic monopoles, dipoles and quadrupoles: an experiment revisited. American Journal of Physics, Volume 67, Pages 660-664.

[12] Guilherme Vaz, David Hally, Tobias Huuva, Norbert Bulten, Pol Muller, Paolo Becchi, Jose L. R. Herrer, Stewart Whitworth, Romain Macé and Andrei Korsström, 2015. Cavitating flow calculations for the E779A propeller in open water and behind conditions: code comparison and solution Validation. *Fourth International Symposium on Marine Propulsors. MARINE 2015*.

[13] Min-sheng Zhao, Wei-wen Zhao y De-cheng Wan, 2020. Numerical simulations of propeller cavitation flows based on OpenFOAM. Journal of Hydrodynamics, Volume 32, Pages 1071-1079.

[14] Abolfazl Asnaghi, 2015. Developing computational methods for detailed assessment of cavitation on marine propellers. Department of Shipping and Marine Technology, Chalmers University of Technology.

[15] Young T. Shen and Scott Gowing, 1994. Salt water effects on bubble and sheet cavitation. *The Second International Symposium on Cavitation*, Tokyo, Japan.

[16] Francesco Salvatore, Francisco Pereira, Mario Felli, Danilo Calcagni, Fabio Di Felice, 2006. Description of the INSEAN E779A Propeller Experimental Dataset. *INSEAN – Italian Ship Model Basin.* Institute of Marine Engineering.

[17] SimFlow. *Courant Number in CFD* [online]. Available from: https://sim-flow.com/courant-number-in-cfd/

[18] Wolf Dynamics. *Tips and tricks in OpenFOAM* [online]. Available from:
http://www.wolfdynamics.com/wiki/tipsandtricks.pdf

[19] Wolf Dynamics. *Naval Applications using OpenFOAM technology* [online]. Advanced OpenFOAM Training, 2016. Available from:
http://www.wolfdynamics.com/training/naval/naval_applications.pdf

[20] International Maritime Organization. *IMO and the Sustainable Development Goals* [online]. Available from:
https://www.imo.org/en/MediaCentre/HotTopics/Pages/SustainableDevelopmentGoals.aspx

[21] Yongshuai Wang, Chaohi He, Xincheng Wang, Huaiyu Cheng, Bin Ji, 2023. Influence of skew angle on the cavitation dynamics and induced low-frequency pressure fluctuations around a marine propeller. *Journal of Ocean Engineering*, Volume 227.

[22] Faith Ertinaz, 2014. Hydro-acoustic Simulations using OpenFOAM. ITU AYOC, Milper Pervance Tecknolojileri.

[23] Mohamad Ali Jaafar, Daniel R. Rousse, Stéphane Gibout, Jean-Pierre Bédécarrats, 2017. A review of dendritic growth during solidification: Mathematical modelling and numerical simulations. *Journal of Environmental Management*.

[24] Wahidullah Hakim Safi. *How to decrease the mesh skewness problem in OpenFOAM and other simulation?* ResearchGate [online]. Available from:

https://www.researchgate.net/post/How-to-decrease-the-mesh-skewness-problem-in-OpenFOAM-and-other-simulations

[25] Travis Carrigan, John Crawner and Carolyn Woeber. *What is a good mesh?* Wolf Dynamics [online]. Available from:

http://www.wolfdynamics.com/wiki/meshing_preliminaries_and_quality_assessment.pdf

[26] Sunny Jevid. *What are the advantages of using the Gaussian filter for edge detection over other types of windows, such as rectangular or triangular?* Quora [online]. Available from: https://www.quora.com/What-are-the-advantages-of-using-the-Gaussian-filter-for-edge-detection-over-other-types-of-windows-such-as-rectangular-or-triangular

[27] OpenFOAM. *About OpenFOAM* [online]. Available from: https://www.openfoam.com/

[28] Khelifa Hami, 2020. Turbulence Modeling a Review for Different Used Methods. International Journal of Heat and Technology, Volume 39, Pages 227-234.

[29] SimFlow. *interPhaseChangeDyMFoam – OpenFOAM Solver* [online]. Available from: https://help.sim-flow.com/solvers/inter-phase-change-dym-foam

[30] SimScale. *K-Epsilon Turbulence Models* [online]. Available from: https://www.simscale.com/docs/simulation-setup/global-settings/k-epsilon/

[31] Wolf Dynamics. *Dynamic meshes in OpenFOAM* [online]. Available from: http://www.wolfdynamics.com/training/movingbodies/OF2021/dynamicmeshes_2021_OF8.pdf

[32] SimScale. *Pressure Inlet and Pressure Outlet* [online]. Available from:

https://www.simscale.com/docs/simulation-setup/boundary-conditions/pressure-inlet-and-pressure-outlet/

APPENDICES

Appendix 1. Convergence Study without Cavitation

Prior to the cavitation study, a convergence analysis based on open water curves (K_T, K_Q and η_0) of the propeller is carried out, in order to find a minimum number of cells, since a convergence analysis for the cavitation case is computationally infeasible. The propeller performance is resolved by using *pimpleFoam* solver, as explained earlier., and the meshing strategy is the same as in the cavitation case The results are compared with the experimental open water curves provided by INSEAN, shown in Figure 58.
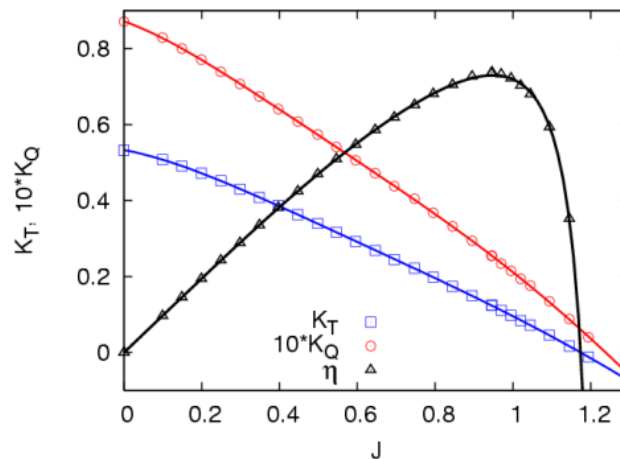
Figure 58. Open-Water Curves of the E779A Propeller, [16]

The test is performed under the same advance coefficient at which the propeller will be studied in the cavitation regime, J = 0.897, although it is performed in open water and at a lower revolution rate, n = 11 rps, so that the inlet flow velocity must be adjusted to V_a = 2.24 m/s. According to the curve above, K_T = 0.152.
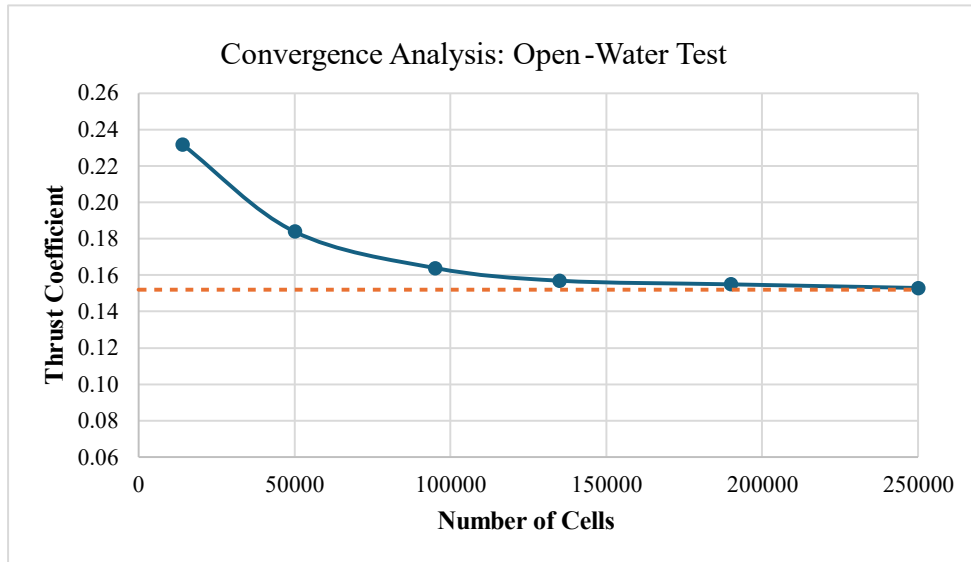
Figure 59. Convergence Study in Open Water Conditions and without Cavitation

The case converges below 1% with 248953 cells, so it is set as a starting point. The mesh obtained in the cavitation case is larger, as it requires more refinement at the inlet to accurately capture the velocity gradients, more refinement in the *innerCylinder* zone to better capture the vapour bubble (it is a more complex problem) and more refinement in the propeller surfaces to well define the edges of the geometry that may affect to the cavitation behaviour.

Table 17. Convergence Study in Open Water Conditions and without Cavitation

Number of Cells	Error (%)
14312	52.63
53275	21.05
95471	7.89
133289	3.29
193428	1.97
248953	0.66

Appendix 2. Velocity Components File

```
# Version of wakeField:  simpleFoam FS wake exported
angle/r      0.9688     1.5500     2.1313     2.7125     3.2937     3.8750     4.4562
  0.00   0.7410   0.1090   0.0250   0.5680  -0.0590   0.0050   0.5390  -0.0520   0.0020   0.5260  -0.0360   0.0010   0.5250  -0.0210   0.0000   0.5380  -0.0060  -0.0000   0.5520   0.0080  -0.0010
 10.00   0.7130   0.0560  -0.1090   0.4930  -0.0370  -0.0030   0.4200  -0.0180   0.0120   0.3960   0.0050   0.0100   0.3820   0.0220   0.0090   0.3820   0.0360   0.0100   0.3900   0.0480   0.0120
 20.00   0.6490  -0.0020  -0.1740   0.4100   0.0010   0.0030   0.3130   0.0220   0.0270   0.2920   0.0380   0.0260   0.2840   0.0510   0.0270   0.2860   0.0610   0.0290   0.2950   0.0670   0.0320
 30.00   0.6110  -0.0220  -0.1650   0.3360   0.0250   0.0170   0.2580   0.0380   0.0420   0.2350   0.0480   0.0460   0.2270   0.0560   0.0480   0.2300   0.0600   0.0510   0.2380   0.0610   0.0530
 40.00   0.5850  -0.0250  -0.1350   0.2830   0.0320   0.0320   0.2210   0.0400   0.0560   0.1970   0.0460   0.0630   0.1890   0.0480   0.0660   0.1900   0.0480   0.0680   0.1940   0.0460   0.0710
 50.00   0.5500  -0.0240  -0.1020   0.2450   0.0290   0.0440   0.1920   0.0340   0.0680   0.1690   0.0350   0.0750   0.1610   0.0330   0.0770   0.1580   0.0300   0.0800   0.1570   0.0260   0.0830
 60.00   0.5020  -0.0220  -0.0740   0.2200   0.0190   0.0530   0.1700   0.0210   0.0760   0.1480   0.0190   0.0810   0.1390   0.0140   0.0830   0.1320   0.0100   0.0850   0.1280   0.0050   0.0870
 70.00   0.4450  -0.0240  -0.0540   0.2010   0.0050   0.0600   0.1530   0.0050   0.0800   0.1340   0.0000   0.0830   0.1230  -0.0050   0.0840   0.1140  -0.0100   0.0850   0.1080  -0.0150   0.0860
 80.00   0.3900  -0.0330  -0.0370   0.1870  -0.0110   0.0640   0.1440  -0.0130   0.0800   0.1250  -0.0180   0.0810   0.1130  -0.0230   0.0810   0.1040  -0.0270   0.0810   0.0970  -0.0320   0.0810
 90.00   0.3520  -0.0430  -0.0240   0.1790  -0.0280   0.0650   0.1380  -0.0300   0.0770   0.1200  -0.0330   0.0760   0.1080  -0.0370   0.0750   0.0980  -0.0400   0.0740   0.0910  -0.0440   0.0730
100.00   0.3300  -0.0520  -0.0150   0.1750  -0.0440   0.0620   0.1350  -0.0440   0.0710   0.1170  -0.0460   0.0700   0.1040  -0.0480   0.0690   0.0950  -0.0510   0.0660   0.0860  -0.0530   0.0650
110.00   0.3170  -0.0640  -0.0080   0.1760  -0.0580   0.0570   0.1350  -0.0570   0.0650   0.1160  -0.0570   0.0630   0.1030  -0.0580   0.0610   0.0920  -0.0590   0.0580   0.0830  -0.0600   0.0550
120.00   0.3130  -0.0750  -0.0060   0.1800  -0.0710   0.0500   0.1360  -0.0690   0.0580   0.1160  -0.0670   0.0550   0.1020  -0.0670   0.0530   0.0910  -0.0670   0.0500   0.0820  -0.0660   0.0470
130.00   0.3250  -0.0810  -0.0050   0.1880  -0.0800   0.0430   0.1380  -0.0770   0.0500   0.1170  -0.0750   0.0470   0.1020  -0.0730   0.0440   0.0900  -0.0720   0.0420   0.0810  -0.0700   0.0400
140.00   0.3460  -0.0850  -0.0070   0.1970  -0.0880   0.0340   0.1410  -0.0860   0.0410   0.1180  -0.0810   0.0380   0.1040  -0.0780   0.0350   0.0910  -0.0760   0.0340   0.0810  -0.0740   0.0320
150.00   0.3640  -0.0940  -0.0090   0.2040  -0.0950   0.0230   0.1460  -0.0920   0.0320   0.1210  -0.0860   0.0300   0.1050  -0.0820   0.0270   0.0920  -0.0780   0.0250   0.0820  -0.0750   0.0240
160.00   0.3660  -0.1130  -0.0100   0.2160  -0.0990   0.0140   0.1510  -0.0960   0.0220   0.1230  -0.0900   0.0210   0.1070  -0.0850   0.0180   0.0940  -0.0800   0.0170   0.0830  -0.0770   0.0160
170.00   0.4100  -0.1030  -0.0040   0.2360  -0.0950   0.0060   0.1590  -0.0960   0.0110   0.1240  -0.0920   0.0110   0.1080  -0.0870   0.0090   0.0950  -0.0810   0.0090   0.0840  -0.0770   0.0080
180.00   0.4580  -0.0850  -0.0010   0.2540  -0.0910  -0.0010   0.1660  -0.0930  -0.0000   0.1260  -0.0920  -0.0000   0.1090  -0.0860  -0.0000   0.0960  -0.0820  -0.0000   0.0840  -0.0780  -0.0000
190.00   0.4100  -0.1030   0.0040   0.2360  -0.0950  -0.0060   0.1590  -0.0960  -0.0110   0.1240  -0.0920  -0.0110   0.1080  -0.0870  -0.0090   0.0950  -0.0810  -0.0090   0.0840  -0.0770  -0.0080
200.00   0.3660  -0.1130   0.0100   0.2160  -0.0990  -0.0140   0.1510  -0.0960  -0.0220   0.1230  -0.0900  -0.0210   0.1070  -0.0850  -0.0180   0.0940  -0.0800  -0.0170   0.0830  -0.0770  -0.0160
210.00   0.3640  -0.0940   0.0090   0.2040  -0.0950  -0.0230   0.1460  -0.0920  -0.0320   0.1210  -0.0860  -0.0300   0.1050  -0.0820  -0.0270   0.0920  -0.0780  -0.0250   0.0820  -0.0750  -0.0240
220.00   0.3460  -0.0850   0.0070   0.1970  -0.0880  -0.0340   0.1410  -0.0860  -0.0410   0.1180  -0.0810  -0.0380   0.1040  -0.0780  -0.0350   0.0910  -0.0760  -0.0340   0.0810  -0.0740  -0.0320
230.00   0.3250  -0.0810   0.0050   0.1880  -0.0800  -0.0430   0.1380  -0.0770  -0.0500   0.1170  -0.0750  -0.0470   0.1020  -0.0730  -0.0440   0.0900  -0.0720  -0.0420   0.0810  -0.0700  -0.0400
240.00   0.3130  -0.0750   0.0060   0.1800  -0.0710  -0.0500   0.1360  -0.0690  -0.0580   0.1160  -0.0670  -0.0550   0.1020  -0.0670  -0.0530   0.0910  -0.0670  -0.0500   0.0820  -0.0660  -0.0470
250.00   0.3170  -0.0640   0.0080   0.1760  -0.0580  -0.0570   0.1350  -0.0570  -0.0650   0.1160  -0.0570  -0.0630   0.1030  -0.0580  -0.0610   0.0920  -0.0590  -0.0580   0.0830  -0.0600  -0.0550
260.00   0.3300  -0.0520   0.0150   0.1750  -0.0440  -0.0620   0.1350  -0.0440  -0.0710   0.1170  -0.0460  -0.0700   0.1040  -0.0480  -0.0690   0.0950  -0.0510  -0.0660   0.0860  -0.0530  -0.0650
270.00   0.3520  -0.0430   0.0240   0.1790  -0.0280  -0.0650   0.1380  -0.0300  -0.0770   0.1200  -0.0330  -0.0760   0.1080  -0.0370  -0.0750   0.0980  -0.0400  -0.0740   0.0910  -0.0440  -0.0730
280.00   0.3900  -0.0330   0.0370   0.1870  -0.0110  -0.0640   0.1440  -0.0130  -0.0800   0.1250  -0.0180  -0.0810   0.1130  -0.0230  -0.0810   0.1040  -0.0270  -0.0810   0.0970  -0.0320  -0.0810
290.00   0.4450  -0.0240   0.0540   0.2010   0.0050  -0.0600   0.1530   0.0050  -0.0800   0.1340   0.0000  -0.0830   0.1230  -0.0050  -0.0840   0.1140  -0.0100  -0.0850   0.1080  -0.0150  -0.0860
300.00   0.5020  -0.0220   0.0740   0.2200   0.0190  -0.0530   0.1700   0.0210  -0.0760   0.1480   0.0190  -0.0810   0.1390   0.0140  -0.0830   0.1320   0.0100  -0.0850   0.1280   0.0050  -0.0870
310.00   0.5500  -0.0240   0.1020   0.2450   0.0290  -0.0440   0.1920   0.0340  -0.0680   0.1690   0.0350  -0.0750   0.1610   0.0330  -0.0770   0.1580   0.0300  -0.0800   0.1570   0.0260  -0.0830
320.00   0.5850  -0.0250   0.1350   0.2830   0.0320  -0.0320   0.2210   0.0400  -0.0560   0.1970   0.0460  -0.0630   0.1890   0.0480  -0.0660   0.1900   0.0480  -0.0680   0.1940   0.0460  -0.0710
330.00   0.6110  -0.0220   0.1650   0.3360   0.0250  -0.0170   0.2580   0.0380  -0.0420   0.2350   0.0480  -0.0460   0.2270   0.0560  -0.0480   0.2300   0.0600  -0.0510   0.2380   0.0610  -0.0530
340.00   0.6490  -0.0020   0.1740   0.4100   0.0010  -0.0030   0.3130   0.0220  -0.0270   0.2920   0.0380  -0.0260   0.2840   0.0510  -0.0270   0.2860   0.0610  -0.0290   0.2950   0.0670  -0.0320
350.00   0.7130   0.0560   0.1090   0.4930  -0.0370   0.0030   0.4200  -0.0180  -0.0120   0.3960   0.0050  -0.0100   0.3820   0.0220  -0.0090   0.3820   0.0360  -0.0100   0.3900   0.0480  -0.0120
```

Appendix 3. Thrust Coefficients

Based on the pressure field, the forces around the propeller were calculated, and thus the thrust coefficient (K_T) was determined. A variation in the thrust force over time is observed, which is due to the generation and collapse of the cavitation bubble. The maximum thrust coefficient occurs when cavitation is minimal (0 as only occurs in 1 blade), and the minimum thrust coefficient occurs when cavitation is maximal. The data are presented in Table *18*.

$$K_T = \frac{T}{\rho n^2 D^4} \tag{28}$$

Table 18. Thrust Coefficient with Maximum Sheet Cavitation Bubble

Profiles	T [N]	K_T
Conventional Blade	346.53	0.140

Appendix 4. Observations during Thesis Development

As far as radiated noise is concerned, the importance of the geometry of a blade, particularly the skew angle, has been emphasized so far. However, when designing a marine propeller, there are other geometrical parameters which are of paramount importance and which may affect the behaviour of the propeller, both in terms of noise and performance. This is intended to explain the main problem encountered during the development of the work: existence of **cavitation on the pressure face**.

This phenomenon occurred because the geometry was not modelled correctly as the angle of attack had been modified, so that the pitch had been reduced, while the operating conditions were maintained. Figure 60 shows a significant difference in pitch and in angle of attack, where the grey propeller is the one whose geometry is already corrected.
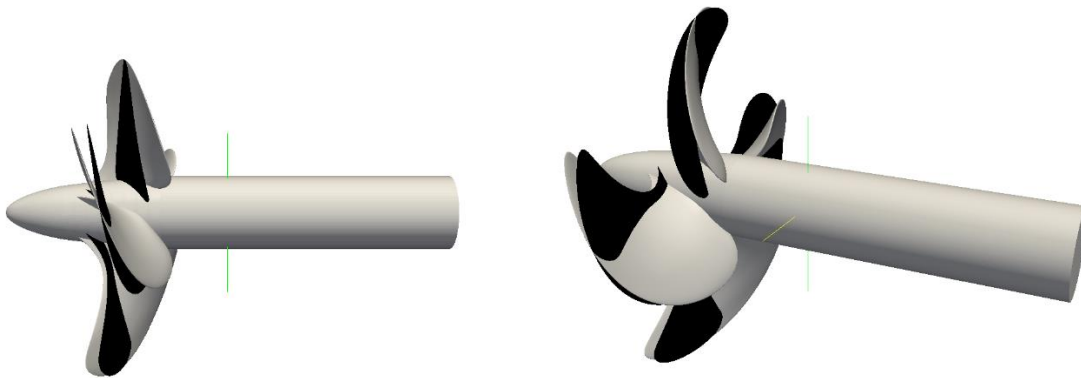
Figure 60. High-Skew Angle Blade Configurations: Low (black) and High (grey) Pitch

The results obtained for this propeller indicate that cavitation is present practically throughout the entire blade path. Two noteworthy aspects are: the cavitation volume curve itself, which suggests that the bubble vibrates, and the area where the phase-change occurs, specifically in the lower region of the pressure face. Nevertheless, the second derivative, and therefore the radiated noise, is lower than in the two previously analysed geometries. The correct approach when dealing with this type of geometry is to change the operating regime by reducing the revolutions.

Appendix 5. OpenFOAM's files required by InterPhaseChangeFoam

Appendix 5.1. ControlDict

```
/*--------------------------------*- C++ -*----------------------------------*\
  =========                 |
  \\      /  F ield          | OpenFOAM: The Open Source CFD Toolbox
   \\    /   O peration       | Website:  https://openfoam.org
    \\  /    A nd             | Version:  8
     \\/     M anipulation    |
\*---------------------------------------------------------------------------*/
FoamFile
{
    version     2.0;
    format      ascii;
    class       dictionary;
    location    "system";
    object      controlDict;
}
// * * * * * * * * * * * * * * * * * * * * * * * * * * * * * * * * * * * * * //
application     interPhaseChangeFoam;
startFrom       latestTime;
startTime       0;
stopAt          endTime;
endTime         0.83;
deltaT          1e-6;
writeControl    adjustableRunTime;
writeInterval   0.001;
purgeWrite      6;
writeFormat     binary;
writePrecision  20;
writeCompression on;
timeFormat      general;
timePrecision   12;
runTimeModifiable true;
adjustTimeStep  yes;
maxCo           0.7;
maxAlphaCo      0.5;
functions
{
    #include "forces"
    waterVolume
    {
        type        volFieldValue;
        libs        ("libfieldFunctionObjects.so");
        log         true;
        writeControl    timeStep;
        writeFields false;
        regionType cellZone;
        name        innerCylinder;
        operation   volIntegrate;
        fields
        (
            alpha.water
        );
    }
```

```
waterVolumeAll
{
      type         volFieldValue;
      libs         ("libfieldFunctionObjects.so");
      log          true;
      writeControl      timeStep;
      writeFields false;
      regionType  cellZone;
       name              CVZone;
      operation   volIntegrate;
      fields
      (
            alpha.water
      );
}
```

```
waterVolumeAll
{
      type         volFieldValue;
      libs         ("libfieldFunctionObjects.so");
      log          true;
      writeControl      timeStep;
      writeFields false;
      regionType  cellZone;
```

Appendix 5.2. fvSchemes

```
/*--------------------------------*- C++ -*----------------------------------*\
  =========                 |
  \\      /  F ield          | OpenFOAM: The Open Source CFD Toolbox
   \\    /   O peration      | Website:  https://openfoam.org
    \\  /    A nd            | Version:  8
     \\/     M anipulation   |
\*---------------------------------------------------------------------------*/
FoamFile
{
    version     2.0;
    format      ascii;
    class       dictionary;
    location    "system";
    object      fvSchemes;
}
// * * * * * * * * * * * * * * * * * * * * * * * * * * * * * * * * * * * * * //
ddtSchemes
{
    default         Euler;
}
gradSchemes
{
    default         Gauss linear;
    grad(U)         cellLimited Gauss linear 1;
}
divSchemes
{
    default             none;
    div(phi,alpha)  Gauss interfaceCompression vanLeer 1;
    div(rhoPhi,U)       Gauss linearUpwind grad(U);
    div(phi,k)          Gauss upwind;
    div(phi,epsilon)    Gauss upwind;
    div(((rho*nuEff)*dev2(T(grad(U))))) Gauss linear;
}
laplacianSchemes
{
    default         Gauss linear limited corrected 0.33;
}
interpolationSchemes
{
    default         linear;
}
snGradSchemes
{
    default         limited corrected 0.33;
}
```

Appendix 5.3. fvSolution

```
/*--------------------------------*- C++ -*----------------------------------*\
  =========                 |
  \\      /  F ield          | OpenFOAM: The Open Source CFD Toolbox
   \\    /   O peration      | Website:  https://openfoam.org
    \\  /    A nd            | Version:  8
     \\/     M anipulation   |
\*---------------------------------------------------------------------------*/
FoamFile
{
    version     2.0;
    format      ascii;
    class       dictionary;
    object      fvSolution;
}
// * * * * * * * * * * * * * * * * * * * * * * * * * * * * * * * * * * * * * //
solvers
{
    "alpha.water.*"
    {
        nAlphaCorr      2;
        nAlphaSubCycles 1;
        MULESCorr       yes;
        nLimiterIter    5;
        solver          smoothSolver;
        smoother        symGaussSeidel;
        tolerance       1e-8;
        relTol          0;
        maxIter         50;
        minIter         1;
    };
    "pcorr.*"
    {
        solver          GAMG;
        tolerance       1e-4;
        relTol          0;
        smoother        DICGaussSeidel;
        cacheAgglomeration no;
            minIter         1;
        maxIter         200;
    }
    p_rgh
    {
        $pcorr;
        tolerance       1e-9;
        relTol          0.01;
    }
    p_rghFinal
    {
        $p_rgh;
        tolerance       1e-9;
        relTol          0;
    }
    "(U|k|epsilon)"
    {
```

```
        solver          smoothSolver;
        smoother        symGaussSeidel;
        tolerance       1e-6;
        relTol          0.01;
        minIter         1;
    }
    "(U|k|epsilon)Final"
    {
        $U;
        relTol          0;
    }
}
PIMPLE
{
    correctPhi          yes;
    nOuterCorrectors    3;
    nCorrectors         2;
    nNonOrthogonalCorrectors 0;
    turbOnFinalIterOnly true;
}
relaxationFactors
{
    "(U|k|epsilon).*"   1;
}
cache
{
    grad(U);
}
```

Appendix 5.4. dynamicMeshDict

```
/*--------------------------------*- C++ -*----------------------------------*\
  =========                 |
  \\      /  F ield         | OpenFOAM: The Open Source CFD Toolbox
   \\    /   O peration     | Website:  https://openfoam.org
    \\  /    A nd           | Version:  8
     \\/     M anipulation  |
\*---------------------------------------------------------------------------*/
FoamFile
{
    version     2.0;
    format      ascii;
    class       dictionary;
    location    "constant";
    object      dynamicMeshDict;
}
// * * * * * * * * * * * * * * * * * * * * * * * * * * * * * * * * * * * * * //
dynamicFvMesh   dynamicMotionSolverFvMesh;
motionSolverLibs ( "libfvMotionSolvers.so" );
motionSolver    solidBody;
cellZone        innerCylinder;
solidBodyMotionFunction  rotatingMotion;
origin      (0 0 0);
axis        (1 0 0);
omega       192; //rad/s
```

Appendix 5.4. transportProperties

```
/*--------------------------------*- C++ -*----------------------------------*\
  =========                 |
  \\      /  F ield         | OpenFOAM: The Open Source CFD Toolbox
   \\    /   O peration     | Website:  https://openfoam.org
    \\  /    A nd           | Version:  8
     \\/     M anipulation  |
\*---------------------------------------------------------------------------*/
FoamFile
{
    version     2.0;
    format      ascii;
    class       dictionary;
    location    "constant";
    object      transportProperties;
}
// * * * * * * * * * * * * * * * * * * * * * * * * * * * * * * * * * * * * //
phases (water vapour);
phaseChangeTwoPhaseMixture SchnerrSauer;
pSat            2300;
sigma           0.07;
water
{
    transportModel  Newtonian;
    nu              1e-06;
    rho             1025;
}
vapour
{
    transportModel Newtonian;
    nu              4.273e-04;
    rho             0.02308;
}
KunzCoeffs
{
    UInf            20.0;
    tInf            0.005;
    Cc              1000;
    Cv              1000;
}
MerkleCoeffs
{
    UInf            20.0;
    tInf            0.005;
    Cc              80;
    Cv              1e-03;
}
SchnerrSauerCoeffs
{
    n               1.6e+13;
    dNuc            2.0e-06;
    Cc              1;
    Cv              1;
}
```

Appendix 5.4. *momentumTransport*

```
/*--------------------------------*- C++ -*----------------------------------*\
  =========                 |
  \\      /  F ield         | OpenFOAM: The Open Source CFD Toolbox
   \\    /   O peration     | Website:  https://openfoam.org
    \\  /    A nd           | Version:  8
     \\/     M anipulation  |
\*---------------------------------------------------------------------------*/
FoamFile
{
    version     2.0;
    format      ascii;
    class       dictionary;
    location    "constant";
    object      momentumTransport;
}
// * * * * * * * * * * * * * * * * * * * * * * * * * * * * * * * * * * * * * //
simulationType  RAS;
RAS
{
    model           kEpsilon;
    turbulence      on;
    printCoeffs     on;
}
```

DECLARATION OF AUTORSHIP

I declare that this thesis and the work presented in it are my own and have been generated by me as the results of my own original research.

Where I have consulted the published work of others, this is always clearly attributed.

Where I have quoted from the work of others, the source is always given. With the exception of such quotations, this thesis is entirely my own work.

I have acknowledged all main sources of help.

Where the thesis is based on work done by myself jointly with others, I have made clear exactly what was done by others and what I have contributed myself.

This thesis contains no material that has been submitted previously, in whole or in part, for the award of any other academic degree or diploma.

I cede copyright of the thesis in favour of the University of Rostock.

Date: 30/07/2024   **Signature**